Recording Fidelity of Relative Paleointensity Characteristics in the North Pacific Ocean

Congcong Gai[1,2,3], Yanguang Liu[4,5], Xuefa Shi[4,5], Chunqing Sun[3], Xiaodong Jiang[1,5], Jianxing Liu[4,5], Yi Zhong[1,5], Qingsong Liu[1,5,6,*]

[1]Centre for Marine Magnetism, Department of Ocean Science and Engineering, Southern University of Science and Technology, Shenzhen, China, [2]Research School of Earth Sciences, Australian National University, Canberra, ACT, Australia, [3]State Key Laboratory of Lithospheric Evolution, Institute of Geology and Geophysics, Chinese Academy of Sciences, Beijing, China, [4]Key Laboratory of Marine Sedimentology and Environmental Geology, First Institute of Oceanography, Ministry of Natural Resources, Qingdao, China, [5]Laboratory for Marine Geology, Qingdao National Laboratory for Marine Science and Technology, Qingdao, China, [6]Southern Marine Science and Engineering Guangdong Laboratory, Guangzhou, China

*Corresponding author: Qingsong Liu (qsliu@sustech.edu.cn)

Key Points:

- We use an age model based on tephra correlation and one radiocarbon date to assess the fidelity of relative paleointensity variations.
- Detrital vortex state and biogenic single domain magnetite are the dominant remanence carriers, and they introduced <0.5-kyr age error.
- Assessment of component-specific magnetic properties should be considered to ensure the reliability of relative paleointensity variations.

Abstract

North Pacific Ocean sediments are important archives of geomagnetic field and paleoenvironmental evolutions, yet late Quaternary sedimentary sequences in the North Pacific Ocean are less explored because of generally low sedimentation rates and the challenge of dating sediments deposited below the calcite compensation depth. Core NP02 sediments from the North Pacific Ocean contain three visible tephra layers, which are identified as the To-Of, Spfa-1, and Kt-3 tephra, respectively. An age model for core NP02 is established based on tephra correlation and one radiocarbon date, which gives a mean sedimentation rate of ~11.6 cm/kyr. Magnetic analyses suggest the dominance of two remanence carriers; detrital vortex state and biogenic single domain magnetite. Variable depth offsets between the relative paleointensity (RPI) signals carried by the two remanence carriers adds a negligible age error (<0.5 kyr) to the core NP02 RPI record. Pronounced RPI amplitude variations are observed, and the Rockall and Laschamp excursions are identified in the core NP02 RPI record based on the age model. The fidelity of the core NP02 RPI record is further verified by comparison with other RPI stacks and records, and we demonstrate that the RPI variations can assist in chronology refinement.

Plain language Summary

The North Pacific Ocean is too deep to preserve materials effectively for the oxygen isotope chronology, and sediments deposit slowly in this region. Therefore, dating is a big problem for late Quaternary sedimentary cores. In this paper, core NP02 sediments from the North Pacific Ocean were studied. The To-Of, Spfa-1, and Kt-3 tephra layers were identified in core NP02 sediments based on the geochemical features. An age model for this core is reconstructed with the aid of tephra ages and one radiocarbon date. Magnetic analyses suggest that both small biogenic

and relatively large detrital magnetite record geomagnetic information, and the two groups of magnetite deposit at about the same time. Based on the age model, core NP02 RPI record preserves the Rockall and Laschamp excursions, and the RPI pattern is consistent with other RPI stacks and records, which verified core NP02 RPI fidelity. Therefore, we demonstrate that RPI variations is a promising dating tool for North Pacific Ocean sediments.

1 Introduction

As the largest ocean in the world, the Pacific Ocean preserves abundant information about geomagnetic field and paleoenvironmental evolutions (e.g., Channell & Lanci, 2014; Doell & Cox, 1971; Dunlea et al., 2017; Jacobel et al., 2017; Lanci et al., 2004; McKinley et al., 2019; Rea et al., 1998; Roberts et al., 1997; Yamazaki & Yamamoto, 2018). However, sedimentation rates in the North Pacific Ocean are generally low (e.g., Korff et al., 2016; Kyte et al., 1993; Ninkovich et al., 1966; Pettke et al., 2000; Prince et al., 1980; Rea et al., 1998), and sediments in this region are usually deposited below the calcite compensation depth (CCD), which impedes development of radiocarbon dating and continuous oxygen-isotope stratigraphy to construct precise age models to assist understanding of late Quaternary geological events. Therefore, a lot of short sedimentary cores in the North Pacific Ocean have been less investigated, and there is an impetus to provide a robust and practical way to date these sediments, and then promote the relevant studies.

Relative paleointensity (RPI) variations of Earth's magnetic field have been used as a chronological tool in marine sediments (e.g., Channell et al., 2009; Channell, Hodell, et al., 2016; Guyodo & Valet, 1996, 1999; Valet et al., 2005; Yamamoto et al., 2007). This makes RPI variations valuable in environments like the deep North Pacific Ocean (Roberts et al., 1997; Shin et al., 2019; Yamamoto et al., 2007; Yamazaki, 1999). The main advantage of the RPI approach is that dipole geomagnetic variations are recorded synchronously around the world and represent a geophysical measurement that is independent of seawater chemistry and that can be used to develop independent age constraints (Roberts et al., 2013). Paleointensity-assisted chronology studies are based on the assumption that sedimentary magnetic records contain information about the magnetic field intensity at the time of sediment deposition (Tauxe, 1993). To ensure that RPI records are not contaminated by other sedimentary magnetic signals, magnetite should be the dominant remanence carrier, the concentration of magnetite should vary down-core by less than one order of magnitude, and the grain size of magnetite should be in the 1-15 μm range (King et al., 1983; Tauxe, 1993). However, these requirements are based on the assumption that sediments contain a single magnetic mineral component rather than a mixture of several components. Recent studies suggest that magnetite with different grain-sizes responds differently to the geomagnetic field during paleomagnetic signal acquisition in sediments (Chen et al., 2017; Ouyang et al., 2014; Roberts et al., 2012, 2013; Yamazaki, Yamamoto, et al., 2013). Biogenic and terrestrial magnetite co-occur pervasively in North Pacific Ocean sediments (Yamazaki & Ioka, 1997; Yamazaki & Shimono, 2013; Q. Zhang et al., 2018). Given that biogenic and terrestrial magnetite have different grain-size distributions, potential complexities in magnetic recording need to be considered, including the possible presence of different remanence acquisition mechanisms with different lock-in depths. Therefore, detailed assessment of magnetic grain-size characteristics should be made to test the fidelity of sedimentary RPI records. In this study, we use an independent age model for North Pacific Ocean core NP02 to assess whether RPI correlations based on magnetite components with different grain-size distributions can be used to refine the core chronology.

2 Materials and Methods

2.1 Core description and sampling

Core NP02 is a 4.35 m gravity piston core from 40.48° N, 150.1° E. It was recovered from the North Pacific Ocean abyssal plain at a water depth of 5,177 m. This location lies below the CCD, so few foraminifera are preserved. The core site is downwind of Asian dust source areas and many volcanoes in the Japanese archipelago and Kamchatka Peninsula (Weber et al., 1996) (Figure 1). Therefore, the studied sediments are composed mainly of clay with occasionally intercalated tephra layers. Cubic samples (8 cm^3) were taken continuously from the working half of core NP02 for paleomagnetic and rock magnetic analyses.

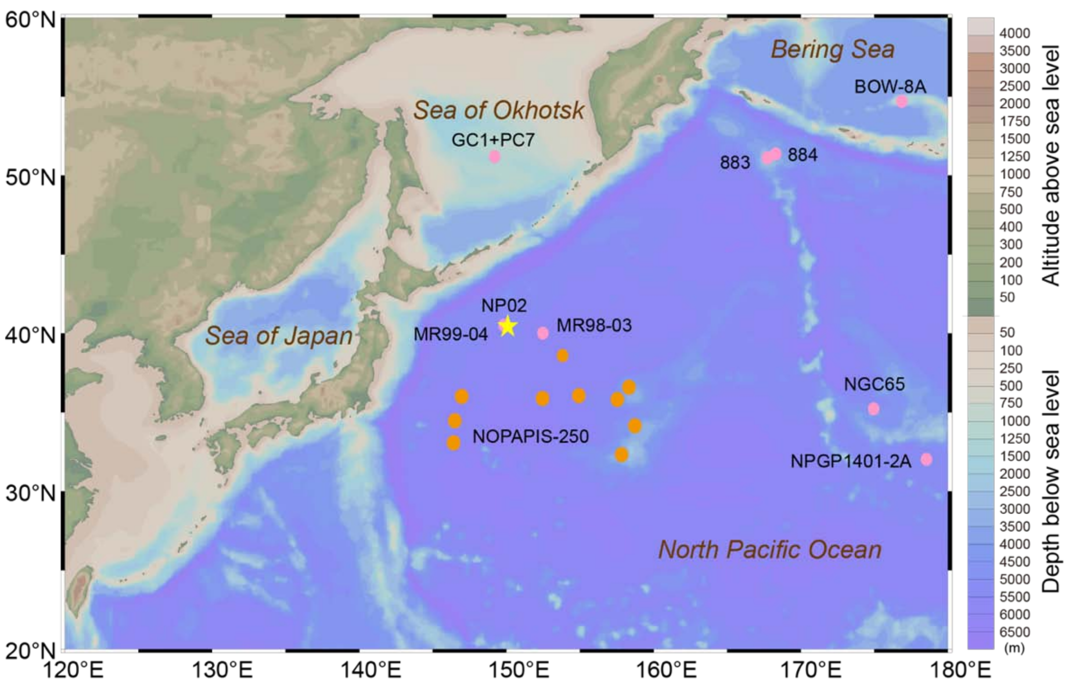

Figure 1. Map of the North Pacific Ocean with locations of core NP02 (yellow star), cores used to develop the NOPAPIS-250 stack (orange circles) (Yamamoto et al., 2007), and other Pacific cores (pink circles) relevant to this study (cores GC1 + PC7, Inoue & Yamazaki, 2010, Yamazaki et al., 2013; core BOW-8A, Okada et al., 2005; Site 883/884, Roberts et al., 1997, Roberts, 2008; MR99-04 and MR98-03, Aoki et al., 2000; core NGC65, Yamazaki, 1999; NPGP1401-2A, Shin et al., 2019).

2.2 Methods

2.2.1 Magnetic measurements

Magnetic remanence measurements were made using a 2-G Enterprises Model 760R cryogenic magnetometer with an in-line alternating field (AF) demagnetizer. The natural remanent magnetization (NRM) was measured and stepwise demagnetized to a peak field of 100 mT, in logarithmically increasing field steps of 0.1-7.7 mT. Characteristic remanent magnetization (ChRM) directions were determined by principal component analysis (PCA) with successive demagnetization points that define vectors directed toward the origin of demagnetization diagrams (Kirschvink, 1980). Core NP02 is not oriented, therefore, the mean ChRM declination was calculated by making a constant azimuthal rotation to all samples to yield an adjusted mean declination of 0°. An anhysteretic remanent magnetization (ARM) was imparted in a 100 mT peak field with a 0.05 mT direct current (DC) bias field, and was then demagnetized with applied fields of 10, 20, 30, 40, 50, 60, 70, 80, 90, and 100 mT. Isothermal magnetizations (IRMs) were imparted in a DC field of 1 T, which is defined here as the saturation IRM (SIRM).

Magnetic susceptibility (χ, mass specific) was measured at a frequency of 976 Hz. Temperature-dependent magnetic susceptibility (χ-T) curves for representative samples were measured in an argon atmosphere from room temperature to 700 °C. χ and χ-T curves were measured using an AGICO Kappabridge MFK 1-FA system equipped with a CS-3 furnace in an argon atmosphere.

IRM acquisition curves and first-order reversal curves (FORCs) (Pike et al., 1999; Roberts et al., 2000) were measured to a maximum field of 1 T using a MicroMag Model 3900 vibrating sample magnetometer. FORC diagrams were processed with the FORCinel software v3.05

(Harrison & Feinberg, 2008), and IRM acquisition curves were decomposed following Robertson and France (1994).

2.2.2 Electron microscope analyses

Magnetic extracts from selected samples were carbon-coated or loaded onto a carbon-coated copper grid for electron microscope analyses. Scan electron microscope (SEM) and transmission electron microscope (TEM)/scanning transmission electron microscope (STEM) observations were made with a PHENOM XL desktop SEM at 15 kV and a F200S S/TEM at 200 kV, respectively. Energy-dispersive X-ray spectroscopy (EDS) analysis was performed to determine the chemical compositions of selected areas semi-quantitatively.

2.2.3 ^{14}C dating

^{14}C dates were obtained using accelerator mass spectrometry on planktonic foraminifera (*N. pachyderma* sinistral). A probability density function of calibrated ages was calculated using ^{14}C determinations and the 1σ range from the Marine13 calibration curve (Reimer et al., 2013) with a reservoir age of ΔR = 400±50 years based on Yoneda et al. (2007). This calibrated age distribution was analyzed subsequently using the Bayesian highest posterior density method to produce a calibrated age range determination following Lougheed and Obrochta (2016).

2.2.4 Volcanic glass shard analysis

Samples from the identified tephra layers were treated with H_2O_2, and then volcanic glass shards were selected, mounted, ground, and polished for electron probe microanalysis. Major element compositions were measured with a JEOL JXA-8100 electron microprobe at 15 kV accelerating voltage with 10 μm beam diameter and 6 nA beam current. Na contents were determined first to reduce the impact of its mobilization. Secondary standard glass, ATHO-G and

StHS6/80-G, were used to check the precesion and accuracy of the data (Jochum et al., 2006). For comparison, all data were normalized to an anhydrous basis (i.e., 100% total oxides).

3 Results

3.1 Paleomagnetic stability

The NRM is demagnetized almost completely at 100 mT (Figure 2a), which suggests that the NRM is carried mainly by low-coercivity magnetic minerals. A secondary remanent magnetization is present in some samples and can be removed by AF demagnetization to 10 mT. ChRMs can be identified as components directed toward the origin of demagnetization diagrams up to 100 mT. Maximum angular deviation (MAD) values were calculated by PCA (Kirschvink, 1980) and are generally < 5° (Figure 2b), which suggests that the ChRMs are stable and well-defined. ChRM inclinations vary about an average value of 52°, which is slightly shallower than the expected geocentric axial dipole value for this site (±59.6°). Shallower inclinations may be associated with acquisition of a depositional remanent magnetization or sediment compaction (Anson & Kodama, 1987; Arason & Levi, 1990; Roberts et al., 2013; Tauxe & Kent, 2004). Three successive reversed polarity inclination values are identified at depths of 39 to 45 cm, which are dinterpreted to represent a geomagnetic excursion.

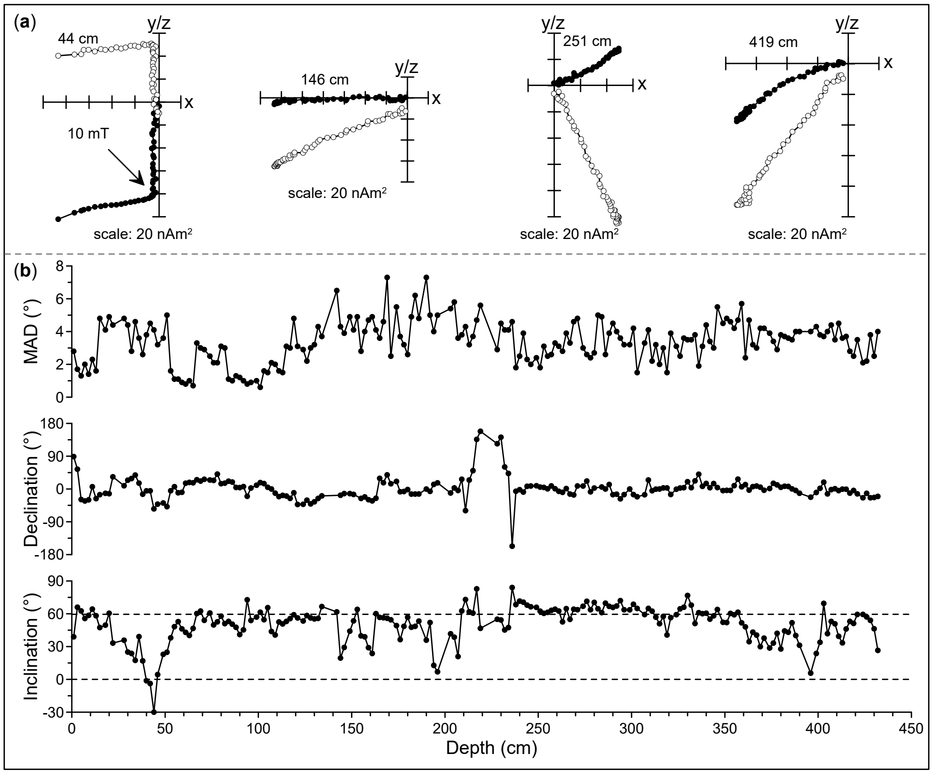

Figure 2. (a) Representative orthogonal projections of AF demagnetization data for sediments from core NP02. Solid (open) circles denote projections of the magnetization vector onto horizontal (vertical) planes. (b) ChRM inclinations, declinations, and MAD values. Dashed lines represent the expected inclination for a geocentric axial dipole field at the site latitude and inclination = 0°, respectively.

3.2 Magnetic mineralogy

Bulk rock magnetic results are shown in Figure 3. χ-T heating curves increase steadily from room temperature to ~300-400 °C (Figure 3a), which indicates gradual unblocking of single domain (SD) particles and/or heating-induced ferrimagnetic mineral neoformation. χ-T curves for tephra-containing samples (i.e., at depths of 141 and 393 cm in Figure 3a) have larger χ values than other curves during both heating and cooling. The heating curve for one tephra-containing sample (141 cm) reaches a near-zero value at ~660 °C, which suggests the presence of hematite. Otherwise, all heating curves decrease to near-zero values at ~580 °C, which corresponds to the

Curie temperature of magnetite (Dunlop & Özdemir, 1997). Down-core variations of concentration-dependent magnetic parameters (χ, ARM, and SIRM) are shown in Figure 3b. Tephra-containing samples are distinguished by anomalously high χ, SIRM, and ARM values, and were removed from our paleomagnetic record. Once these tephra-dominated intervals are removed, χ, ARM, and SIRM values vary within a factor of 5.5, 5.5, and 6.8, respectively, which suggests that the magnetite concentration is relatively homogeneous (i.e. variation of less than one order of magnitude) throughout core NP02. ARM/SIRM is used widely as a magnetic grain-size proxy. However, ARM acquisition can be affected strongly by the magnetic mineral concentration, with higher magnetite concentrations reducing ARM acquisition efficiency (King et al., 1983; Sugiura, 1979). If SIRM is used to represent the magnetic mineral concentration, a higher SIRM should produce lower ARM/SIRM values. A bi-plot of ARM/SIRM and SIRM for core NP02 does not have such a trend (Figure 3c), which indicates that the magnetite concentration has no significant effect on ARM acquisition efficiency. Therefore, ARM/SIRM can be employed here as a magnetic grain-size proxy. A bi-plot of ARM and SIRM has a linear trend with little scatter (Figure 3d), which suggests that changes in bulk magnetite grain size are relatively minor.

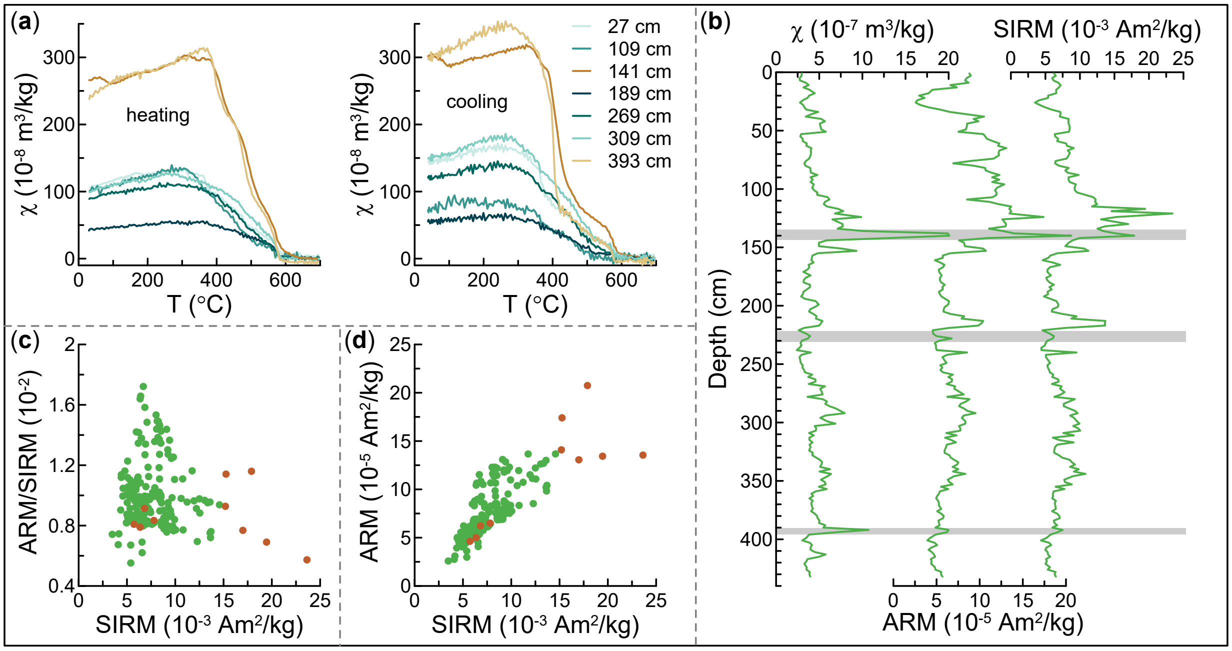

Figure 3. Rock magnetic results from core NP02. (a) Temperature dependence of magnetic susceptibility (χ-T) curves; left (right) are heating (cooling) curves (the depths of the representative samples are indicate in the legend); (b) down-core concentration parameter variations for χ, ARM, and SIRM; major ash layers are indicated by grey shaded areas; (c) bi-plot of SIRM and ARM/SIRM; and (d) bi-plot of SIRM and ARM. Brown circles in (c) and (d) represent volcanic ash-containing samples.

Although the bulk magnetic properties are relatively homogenous, component-specific analyses suggest the presence of mixed magnetic signatures in core NP02. FORC diagrams contain a ridge-like distribution along the B_c axis with little vertical spreading, along with an asymmetrically distributed component that diverges toward the B_u axis (Figures 4a-4f). The former component together with a negative contribution along the B_u axis (Figures 4a-4d) is due to SD particles with uniaxial anisotropy (Muxworthy et al., 2004; Newell, 2005), which is often associated with non-interacting biogenic SD particles (Egli et al., 2010), while the latter component is typical of detrital particles in the magnetic vortex state (Lascu et al., 2018; Muxworthy & Dunlop, 2002; Roberts et al., 2017). On the B_c axis, contours can extend to 110 mT,

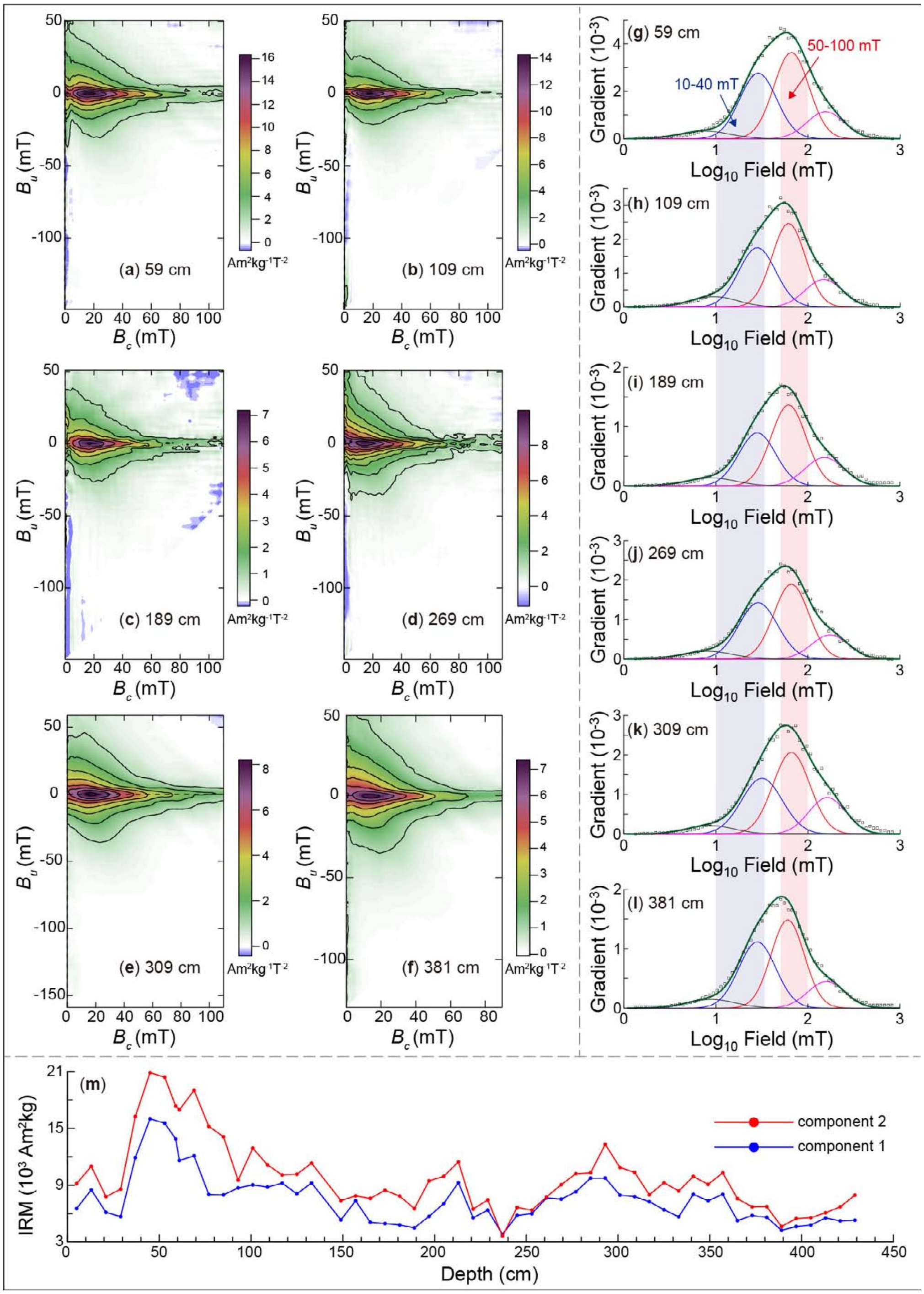

Figure 4. Magnetic properties of typical samples from core NP02. (a-f) FORC diagrams with VARIFORC (Egli, 2013) smoothing parameters of $S_{c,0}$ = 6, $S_{c,1}$ = 9, $S_{b,0}$ = 6, $S_{b,1}$ = 9; (g-l) IRM acquisition curve decomposition. Blue, red, purple, grey, and green curves are for components 1, 2, 3, 4, and the sum of components, respectively; and (m) down-core variations of IRM for components 1 and 2 derived from IRM acquisition curve decomposition.

which indicates the presence of high-coercivity magnetic particles (e.g., Ahmadzadeh et al., 2018; Gai et al., 2020). Some FORC diagrams also contain a secondary peak near the origin (Figures 4a, 4b, and 4d), which indicates viscous behaviour associated with particles near the superparamagnetic/stable SD (SP/SSD) threshold size (Pike et al., 2001; Roberts et al., 2000). Magnetic particles in different grain sizes were verified by the electron microscopic observations, which can be interpreted as detrital vortex and biogenic SD magnetic particles based on their characteristic morphologies and grain sizes (Figure 5). Magnetite seen in SEM images are submicrons to several microns in length, and their shapes are irregular, which are typical of detrital origin (e.g., Ao et al., 2012) (Figure 5e-5g). In comparison, biogenic magnetite seen in TEM images are several tens of nanometers, which are within the SD range. They are evidenced by the regular elongated or equant morphologies (Figure 5a-5d), and by the intact magnetosome chain structure (Figure 5b). Apart from the biogenic magnetite, SD magnetite in TEM images are also occurred as inclusions within detrital silicate host; these magnetic inclusions are clustered (Figure 5h, 5j) or dentritic textures (Figure 5i). For IRM acquisition curves, samples were not saturated at the field of 300 mT, which suggests the presence of high-coercivity magnetic minerals (Figure S1); the asymmetric gradient (Figures 4g-4l) suggests a mixing of multiple coercivity/mineral phases that is consistent with indications from the FORC diagrams. Four components are identified through IRM acquisition curve decomposition of the selected 51 samples. Component 1 ($B_{1/2}$ = 24-33 mT, DP = 0.20-0.22) and component 2 ($B_{1/2}$ = 54-69 mT, DP = 0.19-0.21) contribute more than 75% of the IRM. Considering that magnetic inclusions in silicates contribute little to remanence in oxic pelagic Pacific sediements (Usui et al., 2018), components 1 and 2 are associated with the detrital vortex state and biogenic SD components indicated in FORC diagrams, respectively. Component 3 ($B_{1/2}$ = 148-182 mT, DP = 0.20-0.23) is similar to the low- and mediumcoercivity components identified in Chinese loess-paleosol sequences (Hu et al., 2013; Spassov et al., 2003; R. Zhang et al., 2016), which is interpreted to represent detrital maghemite and/or pedogenic hematite. Component 4 ($B_{1/2}$ <10 mT, DP = 0.26-0.27) may represent pedogenic magnetic particles just above the SP/SSD threshold size, which correspond to the component indicated by the secondary peak at the origin of FORC diagrams. Downcore, IRMs of components 1 and 2 vary within a factor of 4.2 and 5.8, respectively (Figure 4m).

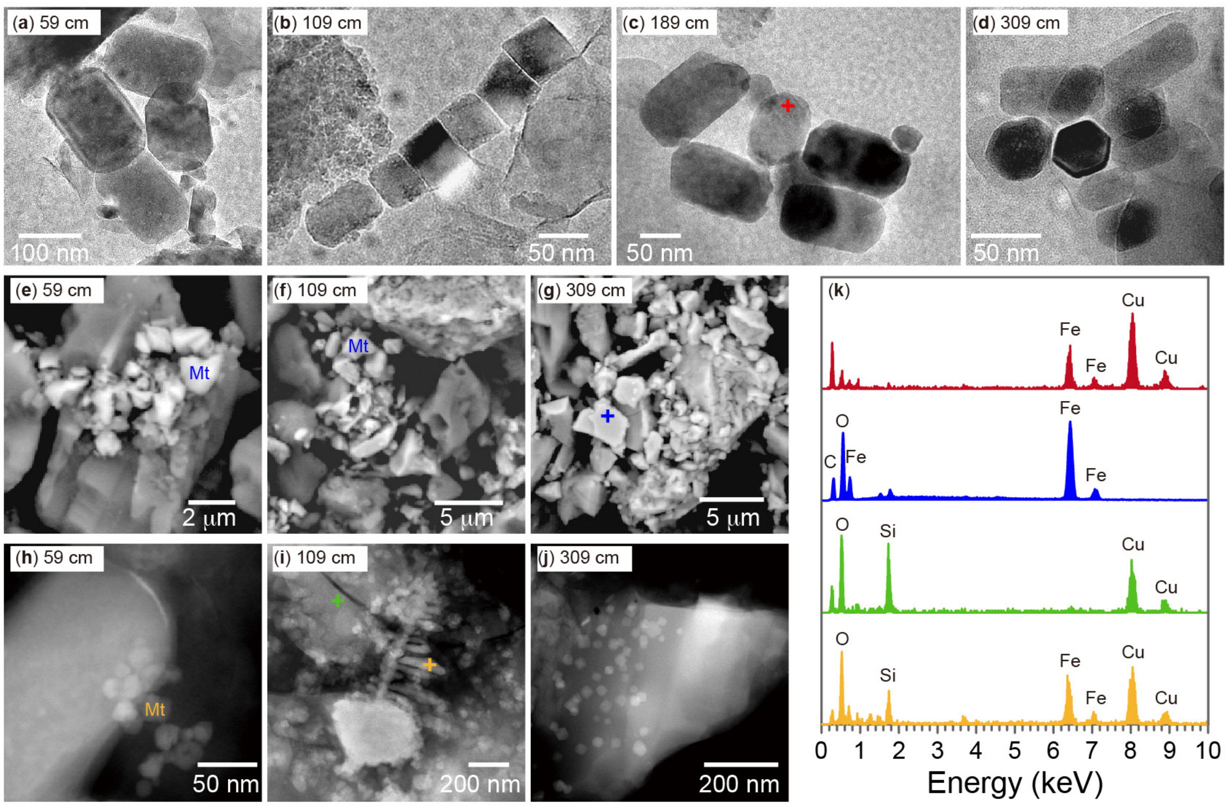

Figure 5. Electron microscope images of particles in magnetic extracts from core NP02. (a-d) TEM images for biogenic magnetite; (e-g) SEM images for detrital magnetite; and (h-j) STEM images for magnetic inclusions within silicates. Red (c), blue (g), green and orange (i) crosses indicate selected areas for EDS analysis, which is presented in (k). EDS analysis indicates that magnetic inclusions and their hosts are magnetite (orange spectrum) and silicates (green spectrum), respectively. The Cu peaks originate from the TEM copper grid. Magnetite particles identified by "Mt" have been verified via EDS.

3.3 Normalized remanence records

RPI values can be estimated by normalizing the NRM by a laboratory-induced magnetization, such as IRM or ARM, to compensate for magnetic mineral concentration changes. Selection of a suitable RPI normalizer depends largely on the grain size distribution of the remanence carrier. ARM is mainly carried by finer magnetic particles, while IRM is also carried by coarser MD particles. Core NP02 samples are dominated by fine (SD and vortex state) magnetic particles, so ARM is chosen as the normalizer.

Our paleomagnetic and rock magnetic results satisfy conventional criteria for RPI studies (King et al., 1983; Tauxe, 1993), and further indicate that two components (hypothesized to be detrital and biogenic magnetite) with different magnetic grain size distributions dominate the magnetic mineral assemblage. The coercivities of the detrital and biogenic components do not overlap strongly over the 10-40 and 50-100 mT windows (blue and pink bands, respectively, in Figures 4g-4l). Therefore, demagnetization intervals of 10-40 and 50-100 mT are chosen to evaluate RPI signals recorded by the detrital and biogenic components, respectively. Due to the logarithmic spacing of demagnetization steps, the 10-40 mT and 50-100 mT demagnetization intervals are represented by the 10.7-41.6 mT and 52.8-100 mT measurements, respectively. The slopes of NRM/ARM derived for the detrital and biogenic components have similar RPI variations (Figure 6a), which indicates that a robust RPI signal is likely to have been recorded in core NP02 sediments, despite the presence of two magnetite sub-populations.

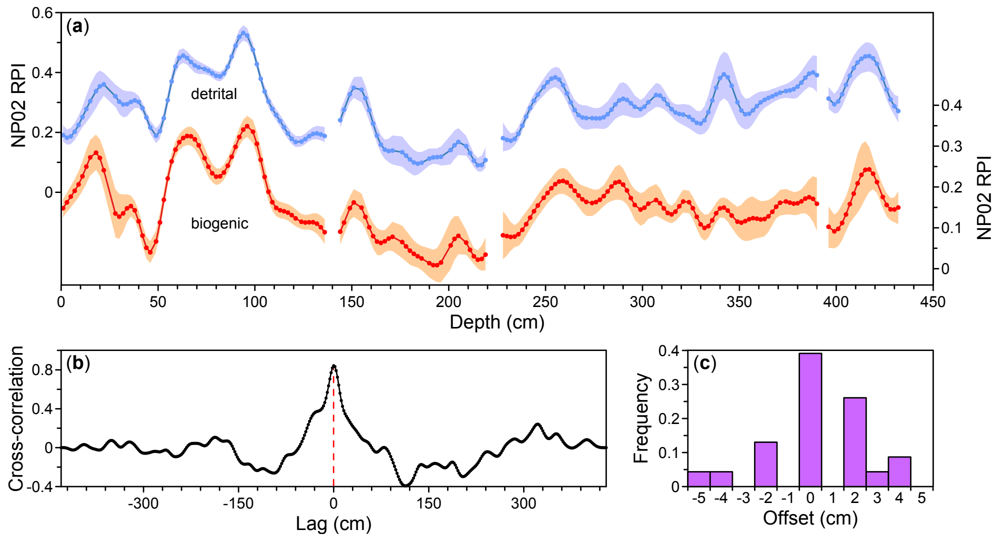

Figure 6. RPI estimates in core NP02. (a) RPI estimates from the detrital ($NRM_{10\text{-}40\ mT}/ARM_{10\text{-}40\ mT}$, blue curve) and biogenic ($NRM_{50\text{-}100\ mT}/ARM_{50\text{-}100\ mT}$, red curve) components with 95% confidence interval, respectively (filtered with a 15 cm cutoff); (b) cross-correlation results for the detrital and biogenic RPI estimates; and (c) distribution of relative offsets between the positions of peaks and troughs in detrital and biogenic RPI estimates.

3.4 Major element composition of glass shards

Three visible tephra layers are identified at depths of 137-143 cm, 220-227 cm, and 391-395 cm. Each tephra layer has homogeneous glass populations with relatively narrow compositional ranges (Figure 7), which excludes the possibility of tephra mixing due to bioturbation and/or simultaneous deposition. Major element compositions of the 34 analyzed glass shards fall into the rhyolite field (Figure 7a). In terms of potassium contents, tephra layers 1 (137-143 cm) and 3 (391-395 cm) belong to the low-K field while tephra layer 2 (220-227 cm) falls into the medium-K field (Figure 7b).

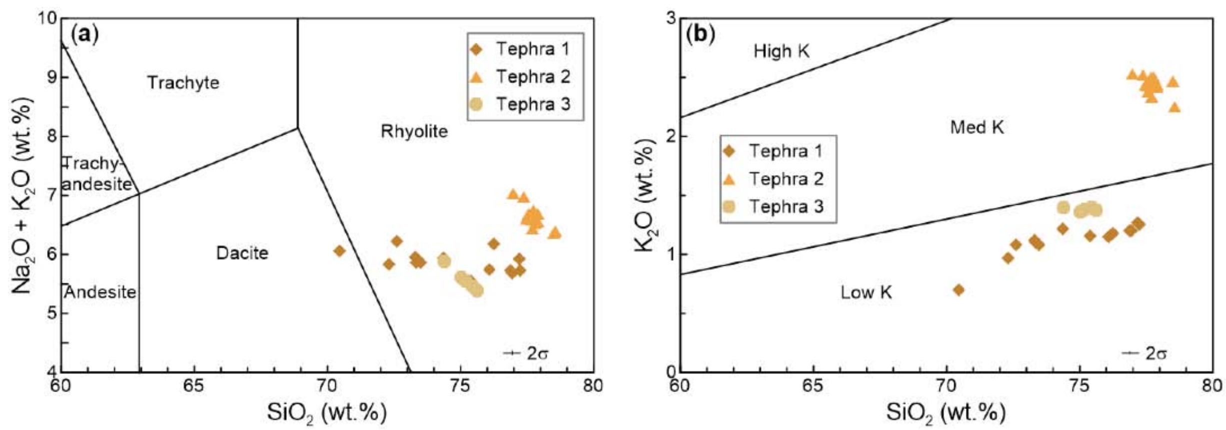

Figure 7. Geochemical characteristics of the glass shards from core NP02. (a) Classification of the total alkali-silica (TAS) diagram with composition fields from Le Bas et al. (1986); and (b) SiO_2-K_2O diagram with boundaries of high-, moderate, and low-K rocks according to Gill (1981). Error bars (2σ) for the glass shards were calculated from the secondary glass standard (AHO-G).

4 Discussion

4.1 Age model construction

Age models are often constructed using interpolation/regression techniques, which assume symmetrically/normally distributed age errors (Blaauw, 2010). However, ^{14}C calibrations often result in asymmetrical and multi-peaked calendar age uncertainties (Blaauw, 2010; Buck et al., 1999; Ramsey, 1995), and such asymmetrical distributions can lead to problems for age model construction. Consideration of full probability density functions can avoid such issues when estimating age-depth models (Blaauw & Christen, 2005; Lougheed & Obrochta, 2019; Ramsey, 2008). There is also an inherent depth uncertainty in sampling geological archives. For core NP02, an age model was constructed following Lougheed and Obrochta (2019) using age constraints provided by the tephra correlation and one calibrated ^{14}C age in which probability density functions are used, with incorporation of realistic errors for both age and depth.

Tephra are a product of large and explosive volcanic eruptions, which spread widely over land, sea, and ice. Unless a volcanic ash has been reworked long after deposition, the same tephra layer in different depositional sinks has effectively an identical age — an isochron — to within about a year and is considered to be geologically synchronous (Lowe, 2011). Therefore, tephra layers are excellent stratigraphic markers and are used widely for correlating and dating sedimentary successions (e.g., Grönvold et al., 1995; Mangerud et al., 1984; Matsu'ura et al., 2014; Rutledal et al., 2020; Smith et al., 2013). In the western North Pacific Ocean, tephra layers are generally dominated by vitric material from high-SiO_2 magmas that originated in subduction-related volcanic events from the Japanese archipelago or the Kamchatka Peninsula (Horn et al., 1969; Ninkovich et al., 1966). By comparing glass shard chemistry results with data reported in previous studies, each tephra layer from core NP02 can be correlated with known Japanese sourced tephra markers. Although Na_2O contents do not overlap perfectly, major element compositions of 14 analyzed glass shards for tephra layer 1 are in good agreement with that of the To-Of tephra, which has been dated to occur in late MIS 3 (32-43.2 ka) (Machida & Arai, 2003; Matsu'ura et al., 2014; Smith et al., 2013). The glass shard chemistry of tephra layers 2 and 3 are highly consistent with that of the Spfa-1 and Kt-3 tephra, respectively (Table 1). The Spfa-1 tephra has an AMS ^{14}C age of 45.105 – 46.560 cal. ka BP (Uesawa et al., 2016), while Kt-3 has an uncalibrated AMS ^{14}C age of 54.616 ± 0.857 ka BP (Amma-Miyasaka et al., 2020). These tephra markers have been reported widely in the North Pacific Ocean; co-occurrences of To-Of and Spfa-1 have been reported in cores MR99-K04 and MR98-03 (Aoki, 2000), which are close to core NP02 (Figure 1).

Table 1.

Average Major-element Compositions of Glass Shards from Core NP02 and Correlative Tephra Markers (Normalized).

	Tephra 1		Tephra 2		Tephra 3		To-Of [a]		Spfa-1[a]		Kt-3[a]	
	Avg.	±1σ	Avg.	±1σ	Avg.	±1σ	Avg.	±1σ	Avg.	±1σ	Avg.	±1σ
SiO_2	74.52	2.16	77.74	0.40	75.14	0.48	77.1	0.74	77.36	0.75	74.73	0.45
TiO_2	0.37	0.07	0.14	0.01	0.35	0.02	0.42	0.07	0.15	0.04	0.35	0.03
Al_2O_3	13.83	1.20	12.31	0.24	12.84	0.22	12.65	0.29	12.37	0.48	12.92	0.39
FeO	1.92	0.32	1.48	0.09	2.84	0.04	1.97	0.23	1.47	0.16	2.76	0.16
MnO	0.08	0.08	0.05	0.07	0.08	0.07	0.08	0.06	0.06	0.02	0.10	0.02
MgO	0.51	0.14	0.16	0.03	0.44	0.03	0.40	0.07	0.18	0.06	0.46	0.05
CaO	2.66	0.69	1.45	0.03	2.68	0.04	2.22	0.21	1.57	0.22	2.69	0.21
Na_2O	4.76	0.27	4.20	0.15	4.19	0.18	3.91	0.12	4.10	0.19	4.37	0.17
K_2O	1.12	0.15	2.44	0.07	1.38	0.02	1.25	0.06	2.70	0.12	1.56	0.12
P_2O_5	0.05	0.05	0.03	0.02	0.06	0.03			0.03	0.03	0.06	0.03
Total	100		100		100		100		100		100	
n	14		15		5		15		114		30	

[a]Average compositions of To-Of tephra is from Machida and Arai (2003), Spfa-1 and Kt-3 tephras are from Amma-Miyasaka et al. (2019).

The To-Of tephra does not provide a suitable age constraint for core NP02 because of its large age uncertainty. However, its occurrence suggests that sediments above this layer were deposited after 40 ka, a time when radiocarbon can play a role in chronology development. Therefore, discrete samples (3 cm in size) were taken from the upper 137 cm of core NP02, and were then washed, sieved, and observed under the microscope to seek foraminifera. Foraminifera are generally preserved poorly in sediments deposited below the CCD, and foraminifera (*N. pachyderma* sinistral) were only identified at a depth of 49-52 cm. A sample from this depth yielded a radiocarbon date of 28.413 (28.077-28.714, 2σ) cal. ka BP.

Ages for the upper (above 50 cm) and lower (below 395 cm) parts of core NP02 are estimated by polynomial fitting and linear regression, respectively. Based on upward extrapolation, the age estimate for the core-top (0 cm) is 21.07 ka. An absence of surficial sediments is common for gravity coring where the surface layer is removed by impact of the core on the seafloor (Adelseck & Anderson, 1978; Karlin, 1990; Skinner & McCave, 2003). After removal of 17 cm for the three tephra-containing sediment intervals, which are considered as instantaneous deposits, the mean sedimentation rate for core NP02 based on our age model is ~11.6 cm/kyr (Figure 8).

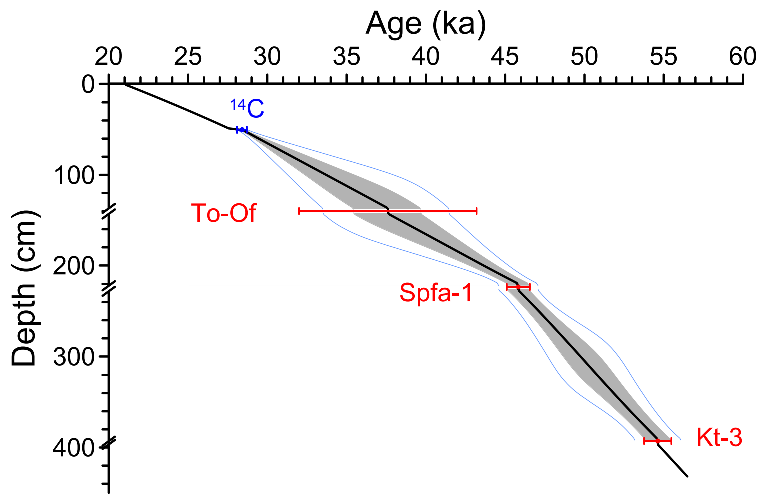

Figure 8. Age-depth model for core NP02. Ages for the upper (<50 cm), intermediate (50-395 cm), and lower (>395 cm) parts are estimated from polynomial fitting, probability density functions (Lougheed and Obrochta, 2019), and linear regression, respectively. Grey shaded areas and blue lines indicate the 1σ and 2σ confidence intervals, respectively. The radiocarbon date and tephra layers with age errors are also indicated.

4.2 Core NP02 RPI characteristics and recording fidelity

Remanence lock-in in sediments can lead to depth offsets between the sediment/water interface and the recorded remanence (Tauxe, 1993; Verosub, 1977). Recent analyses of remanences carried by detrital and biogenic components indicate that there is no relative lock-in depth offset between RPI signals recorded by these components within marine sediments (Chen et al., 2017; Ouyang et al., 2014). For core NP02, cross-correlation results for the detrital and biogenic components suggest no phase lag for the whole sediment sequence (Figure 6b). When comparing the depth positions of all RPI maxima and minima in the sequence, the distribution of relative lock-in depth offsets is centered on zero offset (Figure 6c), which is consistent with the cross-correlation results. However, relative lock-in variations produce a maximum depth error of 5 cm (Figure 6c). For continuous high-resolution RPI studies, any relative lock-in depth offsets could be a crucial limitation when assessing leads and lags between millennial scale climatic variations and, therefore, should be considered as part of the age uncertainty (Roberts et al., 2013). The relative depth offset induces an age error <0.5 kyr for points in the RPI record from core NP02, which should have little effect on comparisons with other RPI stacks/records. Moreover, there is no significant coherence between the RPI estimates and the normalizers, which suggests that sedimentary and/or environmental modulation of the RPI signals were negligible (Figure S2).

Core NP02 RPI estimates are plotted with respect to age in Figure 9a. The RPI minima centered at ~27 ka and ~43 ka in core NP02 are accompanied by aberrant inclinations (Figure S3), which are likely associated with the Rockall and Laschamp excursions (Bonhommet & Babkine, 1967; Bonhommet & Zähringer, 1969; Channell, Harrison, et al., 2016). The Laschamp excursion is the most pervasively documented and studied Quaternary geomagnetic excursion, which occurred at ~41 ka and lasted less than 3 kyr (Laj et al., 2000; Wagner et al., 2000). During the Laschamp excursion, inclination directional changes have been observed from locations with a broad geographical coverage (e.g., Caricchi et al., 2019; Ferk & Leonhardt, 2009; Laj et al., 2006 and references therein; Nowaczyk et al., 2012). However, geomagnetic field behaviour during the Laschamp excursion over the North Pacific Ocean seems to have been different from that over the rest of the world; reversed polarity inclinations have not been recorded in NP02 (Figure S3) and other North Pacific Ocean cores (e.g., Inoue & Yamazaki, 2010; Okada et al., 2005; Roberts et al., 1997; Shin et al., 2019; Xiao et al., 2020; Zhong et al., 2020). Also, a model for the Laschamp excursion predicts that the field intensity over the Pacific Ocean remained relatively high compared to most locations on Earth (Leonhardt et al., 2009). The different geomagnetic field behaviour over the North Pacific Ocean during the Laschamp excursion may have resulted from a relatively large non-dipole to dipole field ratio, which remains to be explored with the aid of higher-resolution records.

Core NP02 RPI variations are compared with global RPI stacks (Sint-2000, PISO-1500, and GLOPIS-75) and regional stacks from the equatorial (West Caroline Basin stack), mid-latitude (the NOPAPIS-250 stack), and subarctic Pacific Ocean (Channell et al., 2009; Laj et al., 2004; Valet et al., 2005; Yamamoto et al., 2007; Yamazaki et al., 2008; Zhong et al., 2020) (Figure 9a). The RPI minimum centered at ~43 ka in core NP02 correlates with the marked RPI Laschamp excursion minimum at ~40-42 ka identified in all other stacks. The lag in recording of this RPI minimum in core NP02 may be due to age model imprecision and/or variable sedimentation rates. Before the Laschamp excursion, all records have broad RPI maxima in the ~47-55 ka interval. After the Laschamp excursion, the records have a generally increasing trend to ~30 ka. Although the reference stacks generally suggest a similar overall pattern, there are still differences in their fine detail. For example, two peaks at ~47 ka and 53 ka occur in the GLOPIS-75 stack, which are not observed in the other stacks that have a broad maximum at ~47-55 ka. Also, the subarctic Pacific stack has larger variations after the Laschamp excursion than the other stacks, particularly

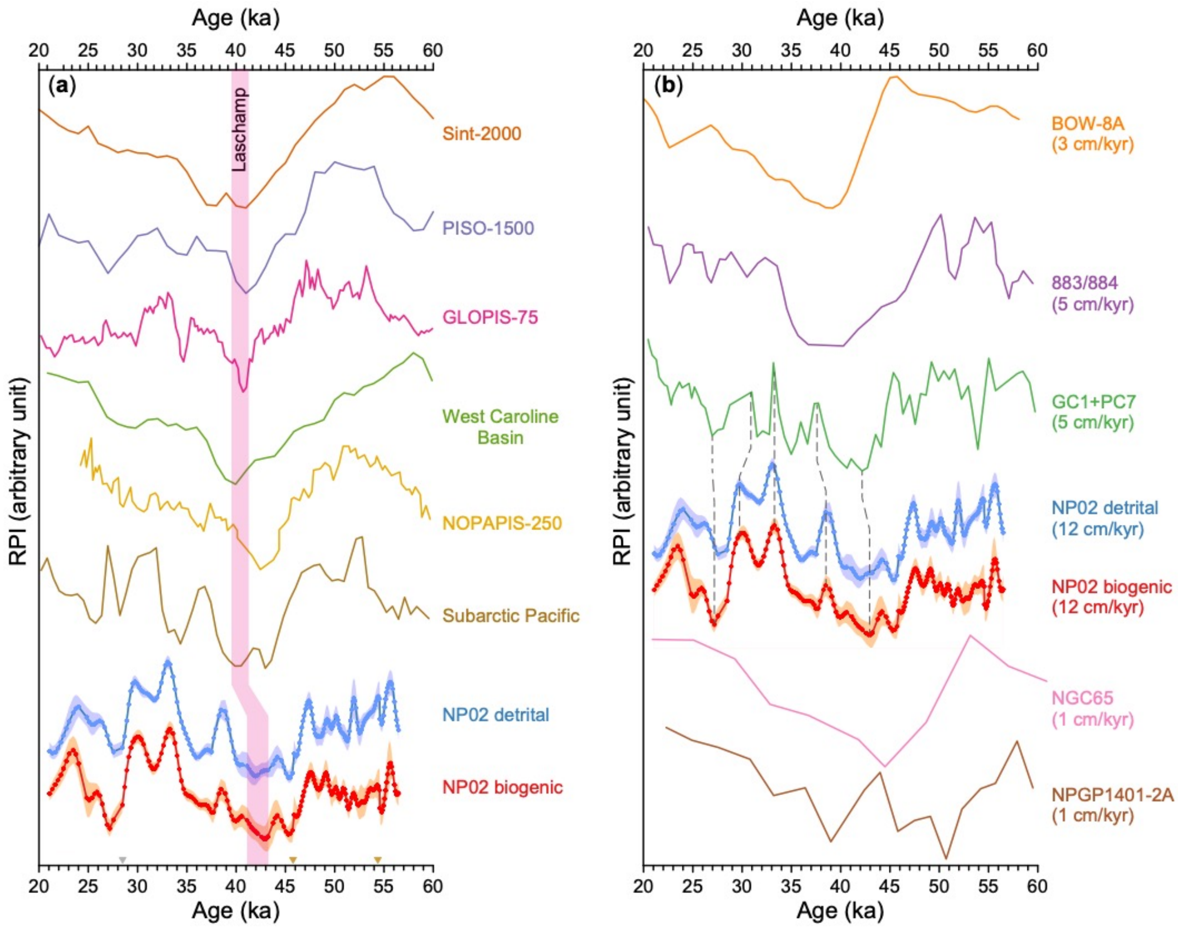

Figure 9. Comparisons of core NP02 RPI estimates with (a) global stacks (Sint-2000 (Valet et al., 2005), PISO-1500 (Channell et al., 2009), and GLOPIS (Laj et al., 2004)); regional stacks from the equatorial (West Caroline Basin stack, Yamazaki et al., 2008), mid-latitude (NOPAPIS-250, Yamamoto et al., 2007), and subarctic Pacific Ocean (Zhong et al., 2020); and (b) individual RPI records of core BOW-8A (Okada et al., 2005), Site 883/884 (Roberts et al., 1997; Roberts, 2008), core GC1+PC7 (Inoue & Yamazaki, 2010; Yamazaki et al., 2013), core NGC65 (Yamazaki, 1999), and core NPGP1401-2A (Shin et al., 2019). The Laschamp excursion is denoted by the pink shaded area. Positions of the radiocarbon date (grey triangle) and tephra layers (brown triangle) from core NP02 are indicated in (a). All stacks and RPI records are rescaled to the 0-1 range. Dashed lines in (b) denote possible correlations between core NP02 and GC1+PC7.

compared to the other regional Pacific stacks. Zhong et al. (2020) attributed the contrasting subarctic North Pacific RPI pattern to regionally variable geomagnetic field behaviour. However, this large variability is not observed in the geomagnetic model of Ziegler and Constable (2015), which covers a longer time duration and suggests lower variability and less significant recording of excursions in the Pacific Ocean compared to the Atlantic Ocean (Ziegler & Constable, 2015). Given that stacking of multiple records with variable resolution can distort amplitude features and smooth high-frequency and local geomagnetic variations, we further compare individual RPI records from the North Pacific Ocean and its marginal seas (Inoue & Yamazaki, 2010; Okada et al., 2005; Roberts, 2008; Roberts et al., 1997; Shin et al., 2019; Yamazaki, 1999; Yamazaki, Inoue, et al., 2013) (Figure 9b). To aid comparison, only records with geomagnetism-independent age models are considered. The RPI record of core NP02 resembles that of GC1+PC7, which validates the core NP02 RPI signal. Apart from this comparison, consistency among individual records is less obvious than among the stacks, which may be associated with age model imprecisions and variable sedimentation rates. Nevertheless, pronounced RPI amplitude variations are recorded at Site 883/884, core GC1+PC7, and core NP02 from mid to high latitudes. In contrast, core BOW-8A from the Bering Sea and cores from latitudes lower than 40° N have less significant amplitude variations, and it is difficult to ascertain whether the lower variability is a result of genuine geomagnetic field behaviour or imperfect recording that smooths the large variability due to low sedimentation rates. The model of Ziegler and Constable (2015) is based mainly on records from the equatorial Pacific Ocean, so their documented low field variability over the Pacific Ocean could be biased; more records from the mid to high latitude Pacific Ocean are required to improve our understanding of Pacific geomagnetic field behaviour.

5 Conclusions

Dating of Quaternary North Pacific Ocean sediments is challenging because they were usually deposited below the CCD. A geomagnetism-independent age model for North Pacific Ocean core NP02 is established with the aid of tephra correlation (using the To-Of, Spfa-1, and Kt-3 tephra layers) and one radiocarbon date. Detrital vortex state and biogenic SD magnetite in sediments from core NP02 both record RPI variations faithfully, which indicates that RPI-assisted chronology is a promising dating tool for North Pacific Ocean sediments. To assess the reliability of RPI determinations, apart from the common criteria suggested by Tauxe (1993), assessment of component-specific magnetic properties, as presented here, is also required. For sediments that contain more than one magnetic mineral component, the RPI record should be checked to ensure that each component records consistent RPI variations. Moreover, relative depth offsets in recording of components needs to be checked to assess whether this provides further age uncertainties that should be taken into consideration.

Acknowledgments

We thank Andrew Roberts and David Heslop for their thoughtful and constructive comments and technical assistance. We thank the anonymous reviewer, the Associate Editor Adrian Muxworthy, and the Editor Mark Dekkers for their valuable comments that improved the paper. This study was supported by the National Natural Science Foundation of China (41874078, 41806063, 41802253, and U1606401), the National Key Research & Development Program of China (2016YFA0601903), Shenzhen Science and Technology Program (KQTD20170810111725321), National Program on Global Change and Air-Sea Interaction (GASI-GEOGE-03), and the Laboratory for Marine Geology, Qingdao Pilot National Laboratory for Marine Science and

Technology (MGQNLM-TD201903). Congcong Gai was further supported by the China Scholarship Council ([2017]3109).

Data availability statement

Data produced in this study are available at Mendeley Data (https://data.mendeley.com/datasets/42pyc27gy7/1) via DOI:10.17632/42pyc27gy7.1.

References

Adelseck Jr, C. G., & Anderson, T. F. (1978). The late Pleistocene record of productivity fluctuations in the eastern equatorial Pacific Ocean. *Geology*, *6*(7), 388–391. https://doi.org/10.1130/0091-7613(1978)6<388:TLPROP>2.0.CO;2

Ahmadzadeh, M., Romero, C., & McCloy, J. (2018). Magnetic analysis of commercial hematite, magnetite, and their mixtures. *AIP Advances*, *8*, 056807. https://doi.org/10.1063/1.5006474

Amma-Miyasaka, M., Miura, D., Nakagawa, M., Uesawa, S., & Furukawa, R. (2020). Stratigraphy and chronology of silicic tephras in the Shikotsu-Toya volcanic field, Japan: evidence of a late Pleistocene ignimbrite flare-up in southwestern Hokkaido. *Quaternary International*, *35*(1–2). https://doi.org/10.1016/j.quaint.2019.11.019

Anson, G. L., & Kodama, K. P. (1987). Compaction-induced inclination shallowing of the post-depositional remanent magnetization in a synthetic sediment. *Geophysical Journal International*, *88*(3), 673–692. https://doi.org/10.1111/j.1365-246X.1987.tb01651.x

Ao, H., An, Z., Dekkers, M. J., Wei, Q., Pei, S., Zhao, H., Zhao, H., Xiao, G., Qiang, X., Wu, D., & Chang, H. (2012). High-resolution record of geomagnetic excursions in the Matuyama chron constrains the ages of the Feiliang and Lanpo Paleolithic sites in the Nihewan Basin, North China. *Geochemistry, Geophysics, Geosystems*, *13*(8). https://doi.org/10.1029/2012GC004095

Aoki, K. (2000). Late Quaternary tephrostratigraphy of marine cores collected during "Mirai" MR98-03 and MR99-K04 cruises. *Report of Japan Marine Science and Technology Center*, *41*, 49–55.

Arason, P., & Levi, S. (1990). Compaction and inclination shallowing in deep-sea sediments from the Pacific Ocean. *Journal of Geophysical Research*, *95*(B4), 4501–4510. https://doi.org/10.1029/JB095iB04p04501

Blaauw, M. (2010). Methods and code for "classical" age-modelling of radiocarbon sequences. *Quaternary Geochronology*, *5*(5), 512–518. https://doi.org/10.1016/j.quageo.2010.01.002

Blaauw, M., & Christen, J. A. (2005). Radiocarbon peat chronologies and environmental change. *Journal of the Royal Statistical Society. Series C: Applied Statistics*, *54*(4), 805–816. https://doi.org/10.1111/j.1467-9876.2005.00516.x

Bonhommet, N., & Babkine, J. (1967). Sur la presence d'aimentation inverse dans la Chaine des Puys. *Comptes Rendus Hebdomadaires Des Seances de l'Academie Des Sciences Series B*, *264*, 92–94.

Bonhommet, N., & Zähringer, J. (1969). Paleomagnetism and potassium argon age determinations of the Laschamp geomagnetic polarity event. *Earth and Planetary Science Letters*, *6*(1), 43–46. https://doi.org/10.1016/0012-821X(69)90159-9

Buck, C., Christen, A., & James, G. N. (1999). BCal: an on-line Bayesian radiocarbon calibration tool. *Internet Archaeology*, *7*. https://doi.org/10.11141/ia.7.1

Caricchi, C., Lucchi, R. G., Sagnotti, L., Macrì, P., Di Roberto, A., Del Carlo, P., Husum, K., Laberg, J. S., & Morigi, C. (2019). A high-resolution geomagnetic relative paleointensity record from the Arctic Ocean deep-water gateway deposits during the last 60 kyr. *Geochemistry, Geophysics, Geosystems*, *20*(5), 2355–2377. https://doi.org/10.1029/2018GC007955

Channell, J. E. T., Harrison, R. J., Lascu, I., McCave, I. N., Hibbert, F. D., & Austin, W. E. N. (2016). Magnetic record of deglaciation using FORC-PCA, sortable-silt grain size, and magnetic excursion at 26 ka, from the Rockall Trough (NE Atlantic). *Geochemistry, Geophysics, Geosystems*, *17*(5), 1823–1841. https://doi.org/10.1002/2016GC006300

Channell, J. E. T., Hodell, D. A., & Curtis, J. H. (2016). Relative paleointensity (RPI) and oxygen isotope stratigraphy at IODP Site U1308: North Atlantic RPI stack for 1.2-2.2 Ma (NARPI-2200) and age of the Olduvai Subchron. *Quaternary Science Reviews*, *131*(Part A), 1–19. https://doi.org/10.1016/j.quascirev.2015.10.011

Channell, J. E. T., & Lanci, L. (2014). Oligocene-Miocene relative (geomagnetic) paleointensity correlated from the equatorial Pacific (IODP Site U1334 and ODP Site 1218) to the South

Atlantic (ODP Site 1090). *Earth and Planetary Science Letters*, *387*, 77–88. https://doi.org/10.1016/j.epsl.2013.11.028

Channell, J. E. T., Xuan, C., & Hodell, D. A. (2009). Stacking paleointensity and oxygen isotope data for the last 1.5 Myr (PISO-1500). *Earth and Planetary Science Letters*, *283*(1–4), 10–23. https://doi.org/10.1016/j.epsl.2009.03.012

Chen, L., Heslop, D., Roberts, A. P., Chang, L., Zhao, X., McGregor, H. V., Marino, G., Rodriguez-Sanz, L., Rohling, E. J., & Pälike, H. (2017). Remanence acquisition efficiency in biogenic and detrital magnetite and recording of geomagnetic paleointensity. *Geochemistry, Geophysics, Geosystems*, *18*(4), 1435–1450. https://doi.org/10.1002/2016GC006753

Doell, R. R., & Cox, A. (1971). Pacific geomagnetic secular variation. *Science*, *171*(3968), 248–254. https://doi.org/10.1126/science.171.3968.248

Dunlea, A. G., Murray, R. W., Santiago Ramos, D. P., & Higgins, J. A. (2017). Cenozoic global cooling and increased seawater Mg/Ca via reduced reverse weathering. *Nature Communications*, *8*(1), 1–7. https://doi.org/10.1038/s41467-017-00853-5

Dunlop, D. J., & Özdemir, Ö. (1997). *Rock Magnetism: Fundamentals and Frontiers*. Cambridge University Press.

Egli, R. (2013). VARIFORC: an optimized protocol for calculating non-regular first-order reversal curve (FORC) diagrams. *Global and Planetary Change*, *110*, 302–320. https://doi.org/10.1016/j.gloplacha.2013.08.003

Egli, R., Chen, A. P., Winklhofer, M., Kodama, K. P., & Horng, C.-S. (2010). Detection of noninteracting single domain particles using first-order reversal curve diagrams. *Geochemistry, Geophysics, Geosystems*, *11*(1). https://doi.org/10.1029/2009gc002916

Ferk, A., & Leonhardt, R. (2009). The Laschamp geomagnetic field excursion recorded in Icelandic lavas. *Physics of the Earth and Planetary Interiors*, *177*(1–2), 19–30. https://doi.org/10.1016/j.pepi.2009.07.011

Gai, C., Liu, Q., Roberts, A. P., Chou, Y., Zhao, X., Jiang, Z., & Liu, J. (2020). East Asian monsoon evolution since the late Miocene from the South China Sea. *Earth and Planetary Science Letters*, *530*, 115960. https://doi.org/10.1016/j.epsl.2019.115960

Gill, J. B. (1981). *Orogenic Andesites and Plate Tectonics*. Springer-Verlag. https://doi.org/10.1016/0377-0273(82)90060-9

Grönvold, K., Óskarsson, N., Johnsen, S. J., Clausen, H. B., Hammer, C. U., Bond, G., & Bard, E.

(1995). Ash layers from Iceland in the Greenland GRIP ice core correlated with oceanic and land sediments. *Earth and Planetary Science Letters*, *135*(1–4), 149–155. https://doi.org/10.1016/0012-821X(95)00145-3

Guyodo, Y., & Valet, J. P. (1996). Relative variations in geomagnetic intensity from sedimentary records: the past 200,000 years. *Earth and Planetary Science Letters*, *143*(1–4), 23–36. https://doi.org/10.1016/0012-821x(96)00121-5

Guyodo, Y., & Valet, J. P. (1999). Global changes in intensity of the Earth's magnetic field during the past 800 kyr. *Nature*, *399*(6733), 249–252. https://doi.org/10.1038/20420

Harrison, R. J., & Feinberg, J. M. (2008). FORCinel: an improved algorithm for calculating first-order reversal curve distributions using locally weighted regression smoothing. *Geochemistry, Geophysics, Geosystems*, *9*(5). https://doi.org/10.1029/2008GC001987

Horn, D. R., Delach, M. N., & Horn, B. M. (1969). Distribution of volcanic ash layers and turbidites in the North Pacific. *Bulletin of the Geological Society of America*, *80*(9), 1715–1724. https://doi.org/10.1130/0016-7606(1969)80[1715:DOVALA]2.0.CO;2

Hu, P., Liu, Q., Torrent, J., Barrón, V., & Jin, C. (2013). Characterizing and quantifying iron oxides in Chinese loess/paleosols: implications for pedogenesis. *Earth and Planetary Science Letters*, *369*, 271–283. https://doi.org/10.1016/j.epsl.2013.03.033

Inoue, S., & Yamazaki, T. (2010). Geomagnetic relative paleointensity chronostratigraphy of sediment cores from the Okhotsk Sea. *Palaeogeography, Palaeoclimatology, Palaeoecology*, *291*(3–4), 253–266. https://doi.org/10.1016/j.palaeo.2010.02.037

Jacobel, A. W., McManus, J. F., Anderson, R. F., & Winckler, G. (2017). Climate-related response of dust flux to the central equatorial Pacific over the past 150 kyr. *Earth and Planetary Science Letters*, *457*, 160–172. https://doi.org/10.1016/j.epsl.2016.09.042

Jochum, K. P., Stoll, B., Herwig, K., Willbold, M., Hofmiann, A. W., Amini, M., et al. (2006). MPI-DING reference glasses for in situ microanalysis: new reference values for element concentrations and isotope ratios. *Geochemistry, Geophysics, Geosystems*, *7*(2). https://doi.org/10.1029/2005GC001060

Karlin, R. (1990). Magnetite diagenesis in marine sediments from the Oregon continental margin. *Journal of Geophysical Research*, *95*(B4), 4405–4419. https://doi.org/10.1029/JB095iB04p04405

King, J. W., Banerjee, S. K., & Marvin, J. (1983). A new rock-magnetic approach to selecting sediments for geomagnetic paleointensity studies: application to paleointensity for the last 4000 years. *Journal of Geophysical Research*, *88*(B7), 5911–5921. https://doi.org/10.1029/JB088iB07p05911

Kirschvink, J. L. (1980). The least-squares line and plane and the analysis of palaeomagnetic data. *Geophysical Journal of the Royal Astronomical Society*, *62*(3), 699–718. https://doi.org/10.1111/j.1365-246X.1980.tb02601.x

Korff, L., von Dobeneck, T., Frederichs, T., Kasten, S., Kuhn, G., Gersonde, R., & Diekmann, B. (2016). Cyclic magnetite dissolution in Pleistocene sediments of the abyssal northwest Pacific Ocean: evidence for glacial oxygen depletion and carbon trapping. *Paleoceanography*, *31*(5), 600–624. https://doi.org/10.1002/2015PA002882

Kyte, F. T., Leinen, M., Heath, G. R., & Zhou, L. (1993). Cenozoic sedimentation history of the central North Pacific: inferences from the elemental geochemistry of core LL44-GPC3. *Geochimica et Cosmochimica Acta*, *57*(8), 1719–1740. https://doi.org/10.1016/0016-7037(93)90109-A

Laj, C., Kissel, C., & Beer, J. (2004). High resolution global paleointensity stack since 75 kyr (GLOPIS-75) calibrated to absolute values. In *Geophysical Monograph Series* (pp. 255–265). AGU. https://doi.org/10.1029/145GM19

Laj, C., Kissel, C., Mazaud, A., Channell, J. E. T., & Beer, J. (2000). North Atlantic palaeointensity stack since 75 ka (NAPIS-75) and the duration of the Laschamp event. *Philosophical Transactions of the Royal Society of London. Series A: Mathematical, Physical and Engineering Sciences*, *358*(1768), 1009–1025. https://doi.org/10.1098/rsta.2000.0571

Laj, C., Kissel, C., & Roberts, A. P. (2006). Geomagnetic field behavior during the Iceland Basin and Laschamp geomagnetic excursions: a simple transitional field geometry? *Geochemistry, Geophysics, Geosystems*, *7*(3). https://doi.org/10.1029/2005GC001122

Lanci, L., Pares, J. M., Channell, J. E. T., & Kent, D. V. (2004). Miocene magnetostratigraphy from equatorial Pacific sediments (ODP Site 1218, Leg 199). *Earth and Planetary Science Letters*, *226*(1–2), 207–224. https://doi.org/10.1016/j.epsl.2004.07.025

Lascu, I., Einsle, J. F., Ball, M. R., & Harrison, R. J. (2018). The vortex state in geologic materials: a micromagnetic perspective. *Journal of Geophysical Research: Solid Earth*, *123*(9), 7285–7304. https://doi.org/10.1029/2018JB015909

Le Bas, M. J., Le Maitre, R. W., Streckeisen, A., & Zanettin, B. (1986). A chemical classification of volcanic rocks based on the total alkali-silica diagram. *Journal of Petrology*, *27*(3), 745–750. https://doi.org/10.1093/petrology/27.3.745

Leonhardt, R., Fabian, K., Winklhofer, M., Ferk, A., Laj, C., & Kissel, C. (2009). Geomagnetic field evolution during the Laschamp excursion. *Earth and Planetary Science Letters*, *278*(1–2), 87–95. https://doi.org/10.1016/j.epsl.2008.11.028

Lougheed, B. C., & Obrochta, S. P. (2016). MatCal: open source Bayesian ^{14}C age calibration in Matlab. *Journal of Open Research Software*, *4*(1). https://doi.org/10.5334/jors.130

Lougheed, B. C., & Obrochta, S. P. (2019). A rapid, deterministic age-depth modeling routine for geological sequences with inherent depth uncertainty. *Paleoceanography and Paleoclimatology*, *34*(1), 122–133. https://doi.org/10.1029/2018PA003457

Lowe, D. J. (2011). Tephrochronology and its application: a review. *Quaternary Geochronology*, *6*(2), 107–153. https://doi.org/https://doi.org/10.1016/j.quageo.2010.08.003

Machida, H., & Arai, F. (2003). *The Atlas of Volcanic Ash*. University of Tokyo Press.

Mangerud, J., Lie, S. E., Furnes, H., Kristiansen, I. L., & Lømo, L. (1984). A Younger Dryas ash bed in western Norway, and its possible correlations with tephra in cores from the Norwegian Sea and the North Atlantic. *Quaternary Research*, *21*(1), 85–104. https://doi.org/10.1016/0033-5894(84)90092-9

Matsu'ura, T., Furusawa, A., Shimogama, K., Goto, N., & Komatsubara, J. (2014). Late Quaternary tephrostratigraphy and cryptotephrostratigraphy of deep-sea sequences (Chikyu C9001C cores) as tools for marine terrace chronology in NE Japan. *Quaternary Geochronology*, *23*, 67–79. https://doi.org/10.1016/j.quageo.2014.06.001

McKinley, C. C., Thomas, D. J., LeVay, L. J., & Rolewicz, Z. (2019). Nd isotopic structure of the Pacific Ocean 40–10 Ma, and evidence for the reorganization of deep North Pacific Ocean circulation between 36 and 25 Ma. *Earth and Planetary Science Letters*, *521*, 139–149. https://doi.org/10.1016/j.epsl.2019.06.009

Muxworthy, A. R., & Dunlop, D. J. (2002). First-order reversal curve (FORC) diagrams for pseudo-single-domain magnetites at high temperature. *Earth and Planetary Science Letters*, *203*(1), 369–382. https://doi.org/10.1016/S0012-821X(02)00880-4

Muxworthy, A. R., Heslop, D., & Williams, W. (2004). Influence of magnetostatic interactions on first-order-reversal-curve (FORC) diagrams: a micromagnetic approach. *Geophysical Journal International*, *158*(3), 888–897. https://doi.org/10.1111/j.1365-246X.2004.02358.x

Newell, A. J. (2005). A high-precision model of first-order reversal curve (FORC) functions for single-domain ferromagnets with uniaxial anisotropy. *Geochemistry, Geophysics, Geosystems*, *6*(5). https://doi.org/10.1029/2004GC000877

Ninkovich, D., Opdyke, N., Heezen, B. C., & Foster, J. H. (1966). Paleomagnetic stratigraphy, rates of deposition and tephrachronology in North Pacific deep-sea sediments. *Earth and Planetary Science Letters*, *1*(6), 476–492. https://doi.org/10.1016/0012-821X(66)90052-5

Nowaczyk, N. R., Arz, H. W., Frank, U., Kind, J., & Plessen, B. (2012). Dynamics of the Laschamp geomagnetic excursion from Black Sea sediments. *Earth and Planetary Science Letters*, *351–352*, 54–69. https://doi.org/10.1016/j.epsl.2012.06.050

Okada, M., Takagi, M., Narita, H., & Takahashi, K. (2005). Chronostratigraphy of sediment cores from the Bering Sea and the subarctic Pacific based on paleomagnetic and oxygen isotopic analyses. *Deep-Sea Research Part II: Topical Studies in Oceanography*, *52*(16–18), 2092–2109. https://doi.org/10.1016/j.dsr2.2005.08.004

Ouyang, T., Heslop, D., Roberts, A. P., Tian, C., Zhu, Z., Qiu, Y., & Peng, X. (2014). Variable remanence acquisition efficiency in sediments containing biogenic and detrital magnetites: implications for relative paleointensity signal recording. *Geochemistry, Geophysics, Geosystems*, *15*(7), 2780–2796. https://doi.org/10.1002/2014GC005301

Pettke, T., Halliday, A. N., Hall, C. M., & Rea, D. K. (2000). Dust production and deposition in Asia and the North Pacific Ocean over the past 12 Myr. *Earth and Planetary Science Letters*, *178*(3–4), 397–413. https://doi.org/10.1016/S0012-821X(00)00083-2

Pike, C. R., Roberts, A. P., & Verosub, K. L. (1999). Characterizing interactions in fine magnetic particle systems using first order reversal curves. *Journal of Applied Physics*, *85*(9), 6660–6667. https://doi.org/10.1063/1.370176

Pike, C. R., Roberts, A. P., & Verosub, K. L. (2001). First-order reversal curve diagrams and thermal relaxation effects in magnetic particles. *Geophysical Journal International*, *145*(3), 721–730. https://doi.org/10.1046/j.0956-540X.2001.01419.x

Prince, R. A., Heath, G. R., & Kominz, M. (1980). Paleomagnetic studies of central North Pacific sediment cores: stratigraphy, sedimentation rates, and the origin of magnetic instability. *Geological Society of America Bulletin*, *91*(8_part_II), 1789–1835. https://doi.org/10.1130/0016-7606(1980)91<447:PSOCNP>2.0.CO;2

Ramsey, C. B. (1995). Radiocarbon calibration and analysis of stratigraphy: the OxCal program.

Radiocarbon, *37*(2), 425–430. https://doi.org/10.1017/s0033822200030903

Ramsey, C. B. (2008). Deposition models for chronological records. *Quaternary Science Reviews*, *27*(1–2), 42–60. https://doi.org/10.1016/j.quascirev.2007.01.019

Rea, D. K., Snoeckx, I., & Joseph, L. H. (1998). Late Cenozoic eolian deposition in the North Pacific: Asian drying, Tibetan uplift, and cooling of the northern hemisphere. *Paleoceanography*, *13*(3), 215–224. https://doi.org/10.1029/98PA00123

Reimer, P. J., Bard, E., Bayliss, A., Beck, J. W., Blackwell, P. G., Ramsey, C. B., Buck, C. E., Cheng, H., Edwards, R. L., Friedrich, M., Grootes, P. M., Guilderson, T. P., Haflidason, H., Hajdas, I., Hatté, C., Heaton, T. J., Hoffmann, D. L., Hogg, A. G., Hughen, K. A., … van der Plicht, J. (2013). IntCal13 and Marine13 radiocarbon age calibration curves 0–50,000 years cal BP. *Radiocarbon*, *55*(4), 1869–1887. https://doi.org/10.2458/azu_js_rc.55.16947

Roberts, A. P. (2008). Geomagnetic excursions: knowns and unknowns. *Geophysical Research Letters*, *35*(17). https://doi.org/10.1029/2008GL034719

Roberts, A. P., Almeida, T. P., Church, N. S., Harrison, R. J., Heslop, D., Li, Y., Li, J., Muxworthy, A. R., Williams, W., & Zhao, X. (2017). Resolving the origin of pseudo-single domain magnetic behavior. *Journal of Geophysical Research: Solid Earth*, *122*(12), 9534–9558. https://doi.org/10.1002/2017JB014860

Roberts, A. P., Chang, L., Heslop, D., Florindo, F., & Larrasoaña, J. C. (2012). Searching for single domain magnetite in the "pseudo-single-domain" sedimentary haystack: implications of biogenic magnetite preservation for sediment magnetism and relative paleointensity determinations. *Journal of Geophysical Research: Solid Earth*, *117*(B8). https://doi.org/10.1029/2012JB009412

Roberts, A. P., Lehman, B., Weeks, R. J., Verosub, K. L., & Laj, C. (1997). Relative paleointensity of the geomagnetic field over the last 200,000 years from ODP Sites 883 and 884, North Pacific Ocean. *Earth and Planetary Science Letters*, *152*(1–4), 11–23. https://doi.org/10.1016/s0012-821x(97)00132-5

Roberts, A. P., Pike, C. R., & Verosub, K. L. (2000). First-order reversal curve diagrams: a new tool for characterizing the magnetic properties of natural samples. *Journal of Geophysical Research: Solid Earth*, *105*(B12), 28461–28475. https://doi.org/10.1029/2000jb900326

Roberts, A. P., Tauxe, L., & Heslop, D. (2013). Magnetic paleointensity stratigraphy and high-resolution Quaternary geochronology: successes and future challenges. *Quaternary Science*

Reviews, *61*(C), 1–16. https://doi.org/10.1016/j.quascirev.2012.10.036

Robertson, D. J., & France, D. E. (1994). Discrimination of remanence-carrying minerals in mixtures, using isothermal remanent magnetisation acquisition curves. *Physics of the Earth and Planetary Interiors*, *82*(3–4), 223–234. https://doi.org/10.1016/0031-9201(94)90074-4

Rutledal, S., Berben, S. M. P., Dokken, T. M., van der Bilt, W. G. M., Cederstrøm, J. M., & Jansen, E. (2020). Tephra horizons identified in the western North Atlantic and Nordic Seas during the Last Glacial Period: extending the marine tephra framework. *Quaternary Science Reviews*, *240*, 106247. https://doi.org/10.1016/j.quascirev.2020.106247

Shin, J. Y., Yu, Y., & Kim, W. (2019). Wavelet-based verification of a relative paleointensity record from the North Pacific. *Earth, Planets and Space*, *71*(1), 88. https://doi.org/10.1186/s40623-019-1067-x

Skinner, L. C., & McCave, I. N. (2003). Analysis and modelling of gravity- and piston coring based on soil mechanics. *Marine Geology*, *199*(1–2), 181–204. https://doi.org/10.1016/S0025-3227(03)00127-0

Smith, V. C., Staff, R. A., Blockley, S. P. E., Ramsey, C. B., Nakagawa, T., Mark, D. F., Takemura, K., & Danhara, T. (2013). Identification and correlation of visible tephras in the Lake Suigetsu SG06 sedimentary archive, Japan: chronostratigraphic markers for synchronising of east Asian/west Pacific palaeoclimatic records across the last 150 ka. *Quaternary Science Reviews*, *67*, 121–137. https://doi.org/10.1016/j.quascirev.2013.01.026

Spassov, S., Heller, F., Kretzschmar, R., Evans, M. E., Yue, L. P., & Nourgaliev, D. K. (2003). Detrital and pedogenic magnetic mineral phases in the loess/palaesol sequence at Lingtai (central Chinese Loess Plateau). *Physics of the Earth and Planetary Interiors*, *140*(4), 255–275. https://doi.org/10.1016/j.pepi.2003.09.003

Sugiura, N. (1979). ARM, TRM and magnetic interactions: concentration dependence. *Earth and Planetary Science Letters*, *42*(3), 451–455. https://doi.org/10.1016/0012-821X(79)90054-2

Tauxe, L. (1993). Sedimentary records of relative paleointensity of the geomagnetic field: theory and practice. *Reviews of Geophysics*, *31*(3), 319–354. https://doi.org/10.1029/93RG01771

Tauxe, L., & Kent, D. V. (2004). A simplified statistical model for the geomagnetic field and the detection of shallow bias in paleomagnetic inclinations: was the ancient magnetic field dipolar? In *Timescales of the Paleomagnetic Field* (pp. 101–115). https://doi.org/10.1029/145GM08

Uesawa, S., Nakagawa, M., & Umetsu, A. (2016). Explosive eruptive activity and temporal magmatic changes at Yotei Volcano during the last 50,000 years, southwest Hokkaido, Japan. *Journal of Volcanology and Geothermal Research*, *325*, 27–44. https://doi.org/10.1016/j.jvolgeores.2016.06.008

Usui, Y., Shimono, T., & Yamazaki, T. (2018). Rock magnetism of quartz and feldspars chemically separated from pelagic red clay: a new approach to provenance study. *Earth, Planets and Space*, *70*(153). https://doi.org/10.1186/s40623-018-0918-1

Valet, J. P., Meynadier, L., & Guyodo, Y. (2005). Geomagnetic dipole strength and reversal rate over the past two million years. *Nature*, *435*(7043), 802–805. https://doi.org/10.1038/nature03674

Verosub, K. L. (1977). Depositional and postdepositional processes in the magnetization of sediments. *Reviews of Geophysics*, *15*(2), 129–143. https://doi.org/10.1029/RG015i002p00129

Wagner, G., Beer, J., Laj, C., Kissel, C., Masarik, J., Muscheler, R., & Synal, H. A. (2000). Chlorine-36 evidence for the Mono Lake event in the summit GRIP ice core. *Earth and Planetary Science Letters*, *181*(1–2), 1–6. https://doi.org/10.1016/S0012-821X(00)00196-5

Weber, E. T., Owen, R. M., Dickens, G. R., Halliday, A. N., Jones, C. E., & Rea, D. K. (1996). Quantitative resolution of eolian continental crustal material and volcanic detritus in North Pacific surface sediment. *Paleoceanography*, *11*(1), 115–127. https://doi.org/10.1029/95PA02720

Xiao, C., Wang, Y., & Lin, J. (2020). Constraints of magnetostratigraphic and mineralogical data on the provenance of sediments in the Parece Vela Basin of the western Pacific. *Journal of Asian Earth Sciences*, *196*, 104373. https://doi.org/10.1016/j.jseaes.2020.104373

Yamamoto, Y., Yamazaki, T., Kanamatsu, T., Ioka, N., & Mishima, T. (2007). Relative paleointensity stack during the last 250 kyr in the northwest Pacific. *Journal of Geophysical Research: Solid Earth*, *112*(1). https://doi.org/10.1029/2006JB004477

Yamazaki, T. (1999). Relative paleointensity of the geomagnetic field during Brunhes Chron recorded in North Pacific deep-sea sediment cores: orbital influence? *Earth and Planetary Science Letters*, *169*(1–2), 23–35. https://doi.org/10.1016/S0012-821X(99)00064-3

Yamazaki, T., Inoue, S., Shimono, T., Sakamoto, T., & Sakai, S. (2013). Sea-ice conditions in the Okhotsk Sea during the last 550 kyr deduced from environmental magnetism. *Geochemistry,* *Geophysics, Geosystems*, *14*(12), 5026–5040. https://doi.org/10.1002/2013GC004959

Yamazaki, T., & Ioka, N. (1997). Environmental rock-magnetism of pelagic clay: implications for Asian eolian input to the North Pacific since the Pliocene. *Paleoceanography*, *12*(1), 111–124. https://doi.org/10.1029/96PA02757

Yamazaki, T., Kanamatsu, T., Mizuno, S., Hokanishi, N., & Gaffar, E. Z. (2008). Geomagnetic field variations during the last 400 kyr in the western equatorial Pacific: paleointensity-inclination correlation revisited. *Geophysical Research Letters*, *35*(20). https://doi.org/10.1029/2008GL035373

Yamazaki, T., & Shimono, T. (2013). Abundant bacterial magnetite occurrence in oxic red clay. *Geology*, *41*(11), 1191–1194. https://doi.org/10.1130/G34782.1

Yamazaki, T., & Yamamoto, Y. (2018). Relative paleointensity and inclination anomaly over the last 8 Myr obtained from the Integrated Ocean Drilling Program Site U1335 sediments in the eastern equatorial Pacific. *Journal of Geophysical Research: Solid Earth*, *123*(9), 7305–7320. https://doi.org/10.1029/2018JB016209

Yamazaki, T., Yamamoto, Y., Acton, G., Guidry, E. P., & Richter, C. (2013). Rock-magnetic artifacts on long-term relative paleointensity variations in sediments. *Geochemistry, Geophysics, Geosystems*, *14*(1), 29–43. https://doi.org/10.1002/ggge.20064

Yoneda, M., Uno, H., Shibata, Y., Suzuki, R., Kumamoto, Y., Yoshida, K., Sasaki, T., Suzuki, A., & Kawahata, H. (2007). Radiocarbon marine reservoir ages in the western Pacific estimated by pre-bomb molluscan shells. *Nuclear Instruments and Methods in Physics Research, Section B*, *259*(1), 432–437. https://doi.org/10.1016/j.nimb.2007.01.184

Zhang, Q., Liu, Q., Li, J., & Sun, Y. (2018). An integrated study of the eolian dust in pelagic sediments from the North Pacific Ocean based on environmental magnetism, transmission electron microscopy, and diffuse reflectance spectroscopy. *Journal of Geophysical Research: Solid Earth*, *123*(5), 3358–3376. https://doi.org/10.1002/2017JB014951

Zhang, R., Necula, C., Heslop, D., & Nie, J. (2016). Unmixing hysteresis loops of the late Miocene-early Pleistocene loess-red clay sequence. *Scientific Reports*, *6*(1), 1–8. https://doi.org/10.1038/srep29515

Zhong, Y., Liu, Y., Yang, X., Zhang, J., Liu, J., Bosin, A., Gorbarenko, S. A., Shi, X., Chen, T., Chou, Y. M., Liu, W., Wang, H., Gai, C., Liu, J., Derkachev, A. N., Qiang, X., & Liu, Q. (2020). Do non-dipole geomagnetic field behaviors persistently exist in the subarctic Pacific

Ocean over the past 140 ka? *Science Bulletin*, *65*(18), 1505–1507. https://doi.org/10.1016/j.scib.2020.05.016

Ziegler, L. B., & Constable, C. G. (2015). Testing the geocentric axial dipole hypothesis using regional paleomagnetic intensity records from 0 to 300 ka. *Earth and Planetary Science Letters*, *423*, 48–56. https://doi.org/10.1016/j.epsl.2015.04.022

Figure 1

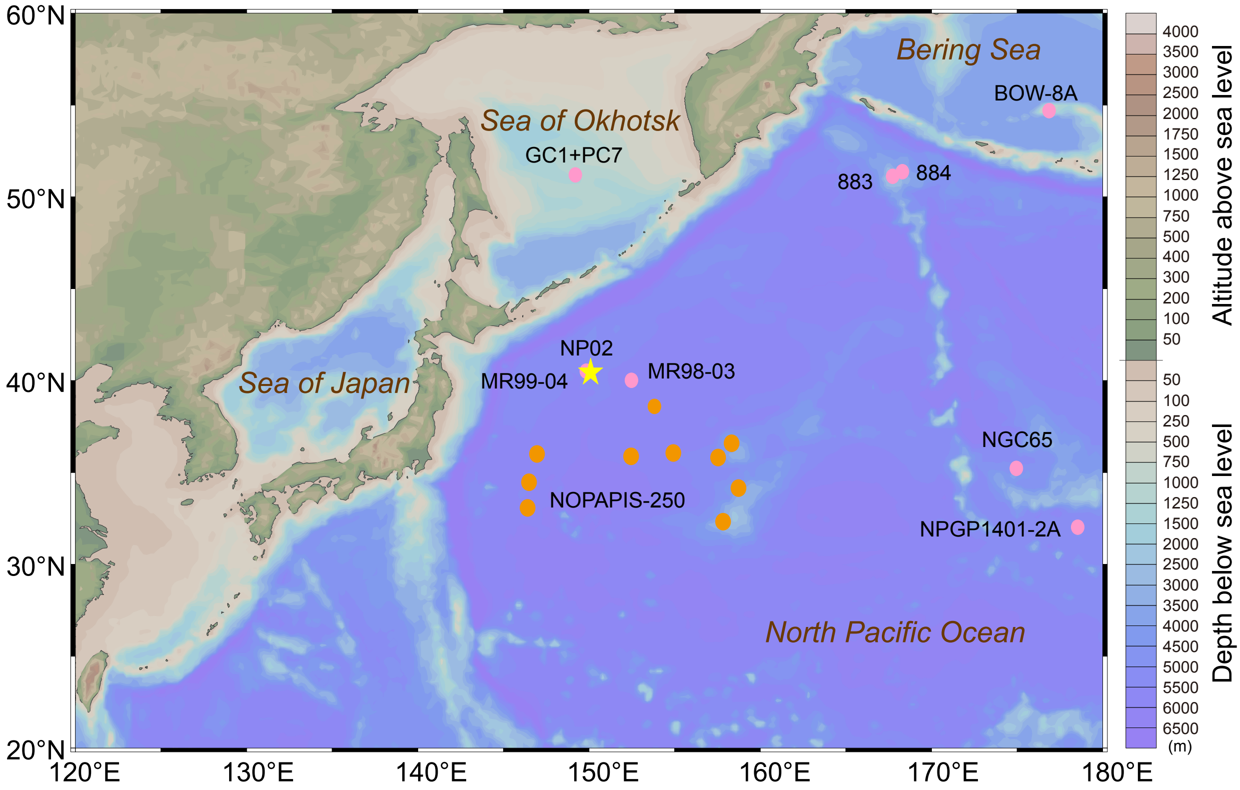

60°N
50°N
40°N
30°N
20°N
120°E
130°E
140°E
150°E
160°E
170°E
180°E
Sea of Okhotsk
Bering Sea
Sea of Japan
North Pacific Ocean
GC1+PC7
BOW-8A
883
884
NP02
MR99-04
MR98-03
NGC65
NOPAPIS-250
NPGP1401-2A
Altitude above sea level
4000
3500
3000
2500
2000
1750
1500
1250
1000
750
500
400
300
200
100
50
Depth below sea level
50
100
250
500
750
1000
1250
1500
2000
2500
3000
3500
4000
4500
5000
5500
6000
6500
(m)

Figure 2

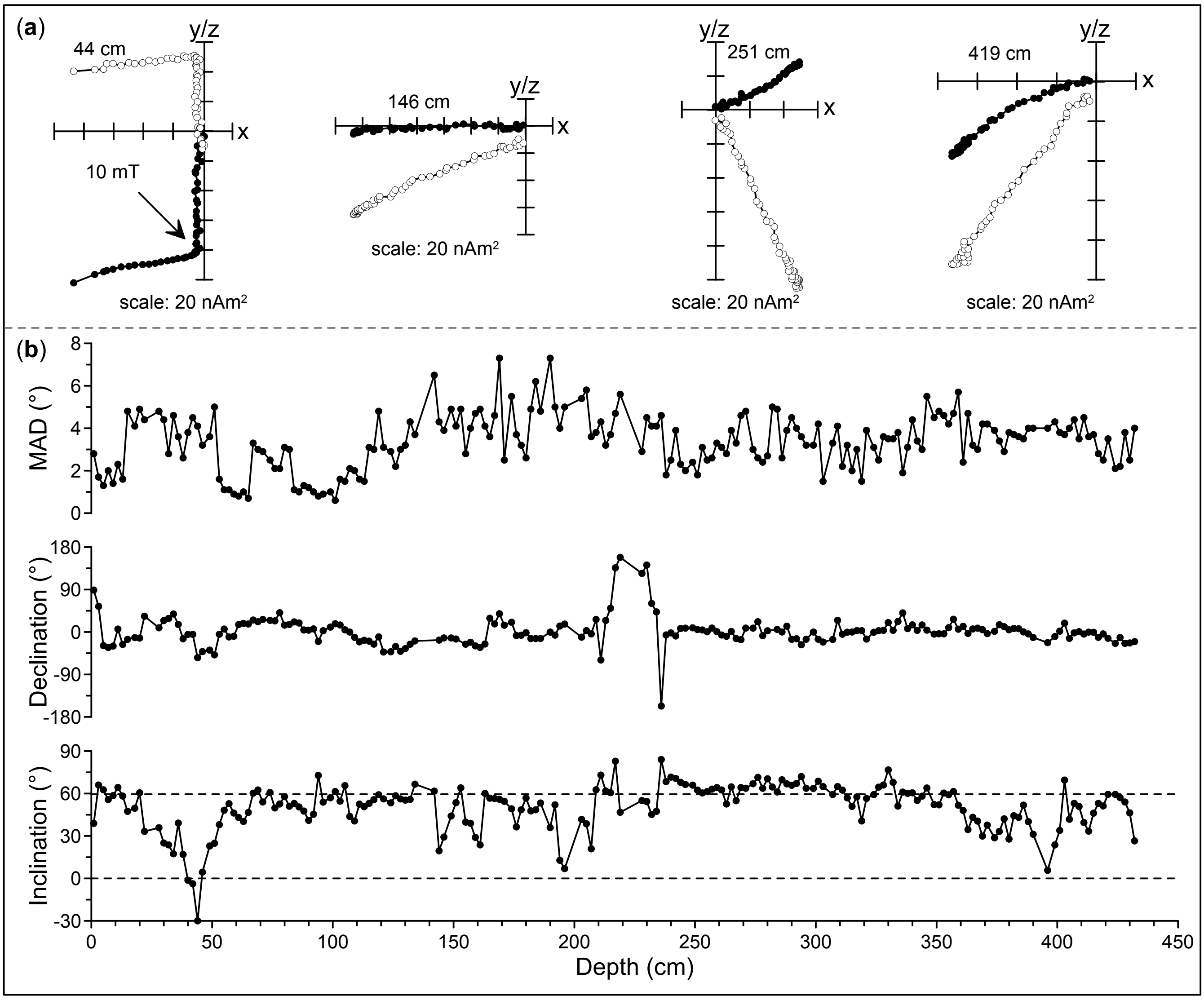
(a)
y/z
44 cm
x
10 mT
scale: 20 nAm²
146 cm
y/z
x
scale: 20 nAm²
y/z
251 cm
x
scale: 20 nAm²
y/z
419 cm
x
scale: 20 nAm²
(b)
MAD (°)
Declination (°)
Inclination (°)
Depth (cm)

Figure 3

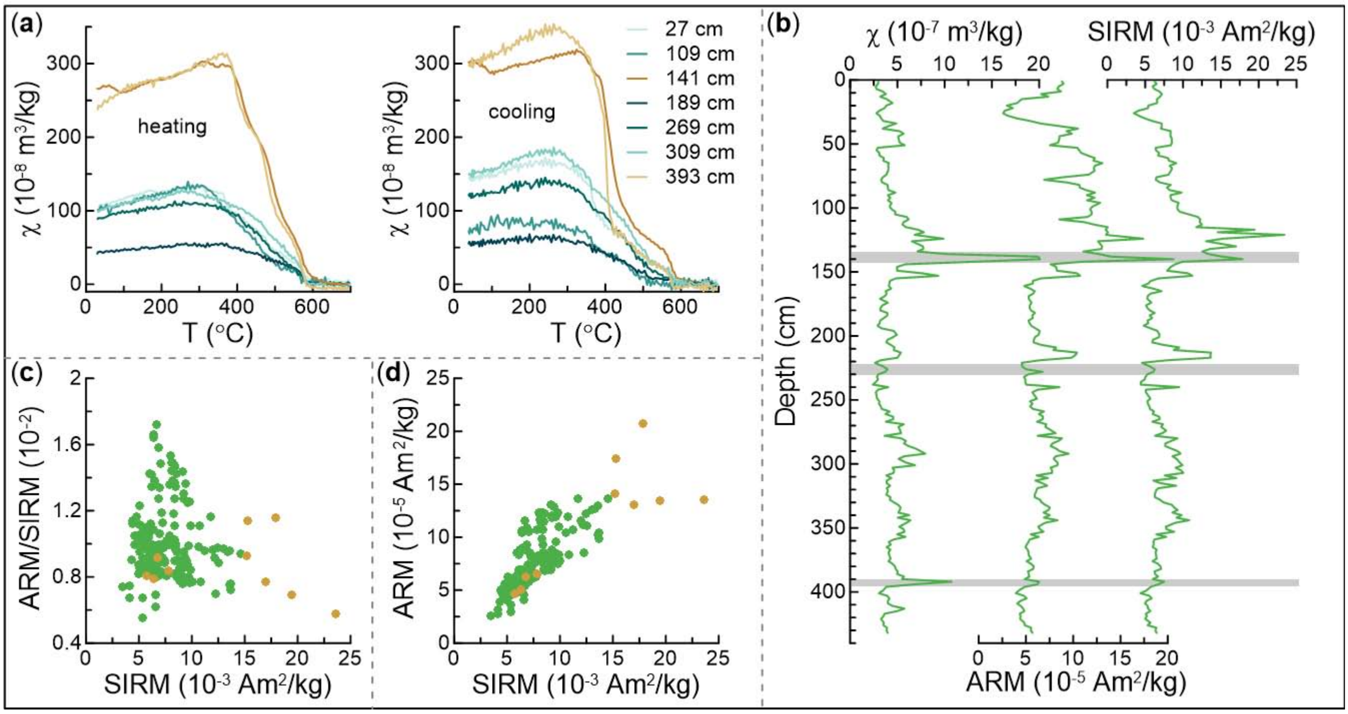
(a)
heating
cooling
χ (10-8 m3/kg)
T (°C)
27 cm
109 cm
141 cm
189 cm
269 cm
309 cm
393 cm
(b)
χ (10-7 m3/kg)
SIRM (10-3 Am2/kg)
Depth (cm)
ARM (10-5 Am2/kg)
(c)
ARM/SIRM (10-2)
SIRM (10-3 Am2/kg)
(d)
ARM (10-5 Am2/kg)
SIRM (10-3 Am2/kg)

Figure 4

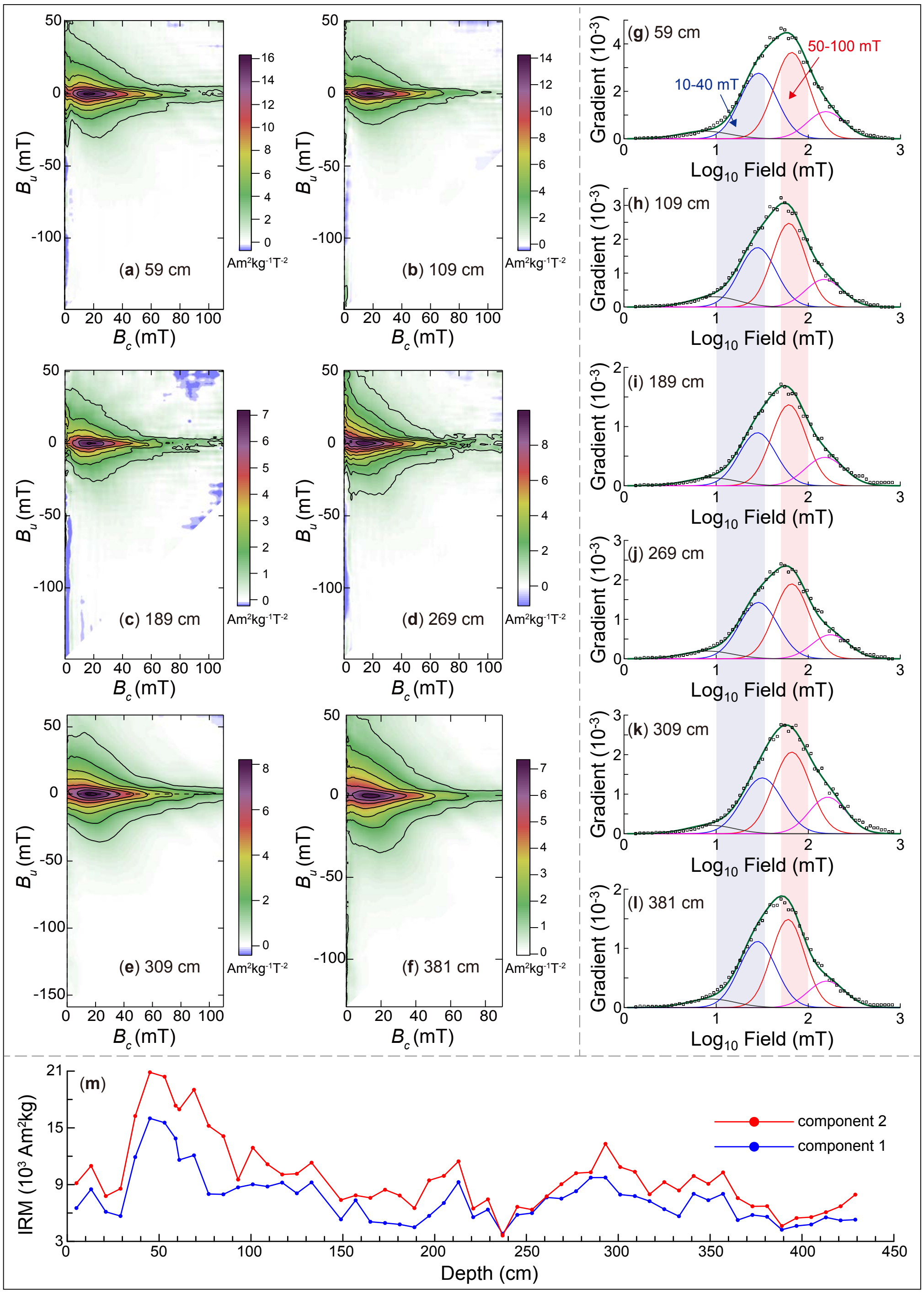

Figure 5

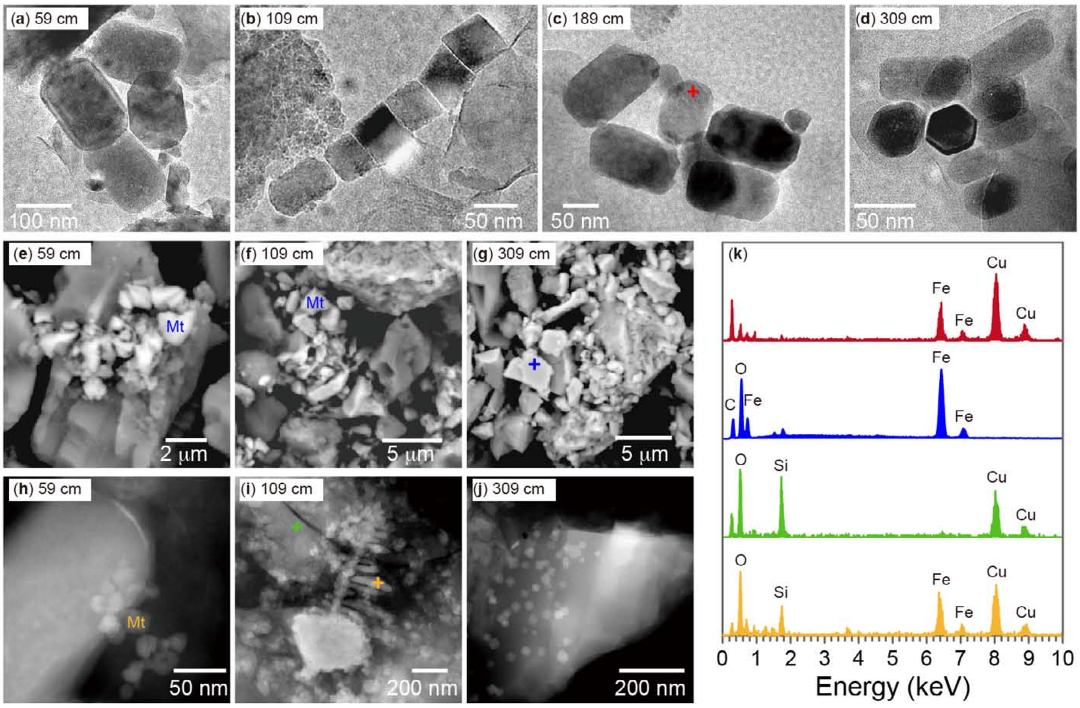
(a) 59 cm
100 nm
(b) 109 cm
50 nm
(c) 189 cm
50 nm
(d) 309 cm
50 nm
(e) 59 cm
Mt
2 μm
(f) 109 cm
Mt
5 μm
(g) 309 cm
5 μm
(h) 59 cm
Mt
50 nm
(i) 109 cm
200 nm
(j) 309 cm
200 nm
(k)
Fe
Cu
Fe
Cu
O
Fe
C
Fe
Fe
O
Si
Cu
Cu
O
Si
Fe
Cu
Fe
Cu
0 1 2 3 4 5 6 7 8 9 10
Energy (keV)

Figure 6

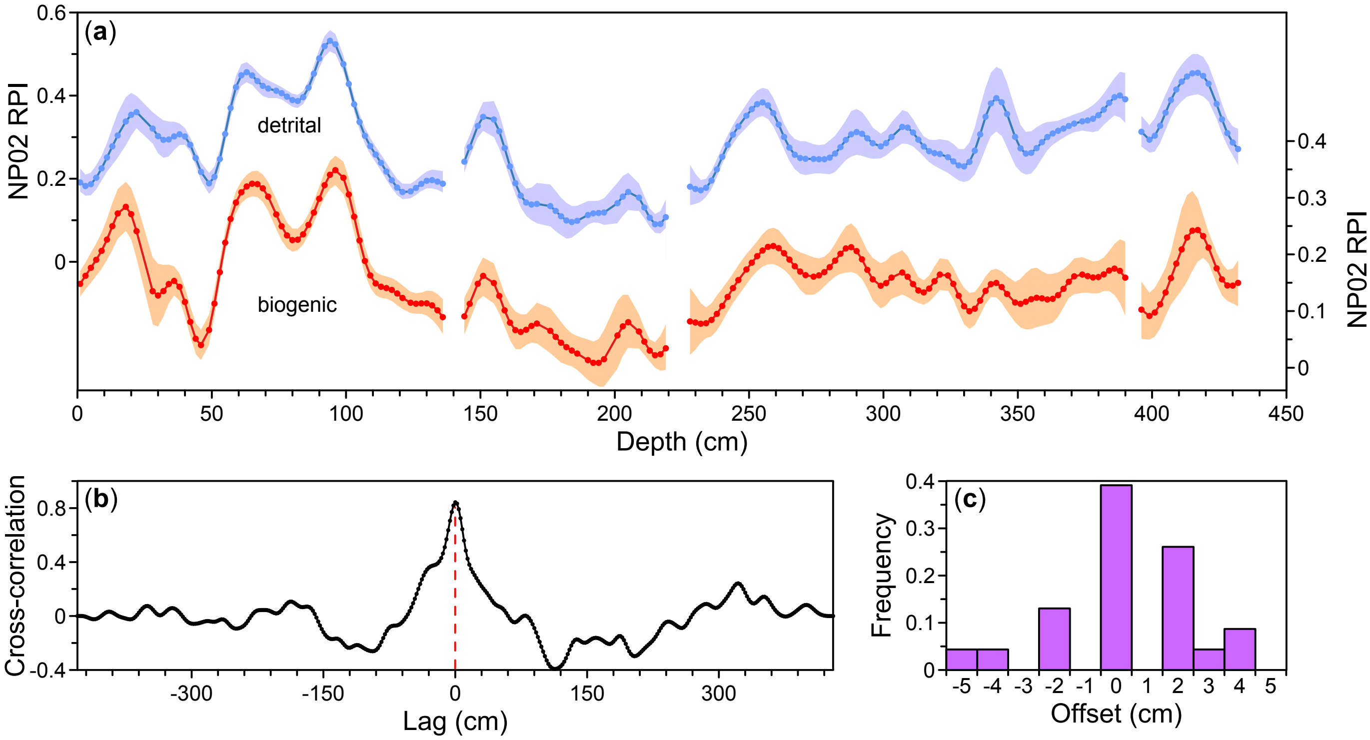
(a)
NP02 RPI
detrital
biogenic
Depth (cm)
0
50
100
150
200
250
300
350
400
450
0.6
0.4
0.2
0
0.4
0.3
0.2
0.1
0
(b)
Cross-correlation
Lag (cm)
0.8
0.4
0
-0.4
-300
-150
0
150
300
(c)
Frequency
Offset (cm)
0.4
0.3
0.2
0.1
0
-5
-4
-3
-2
-1
0
1
2
3
4
5

Figure 7

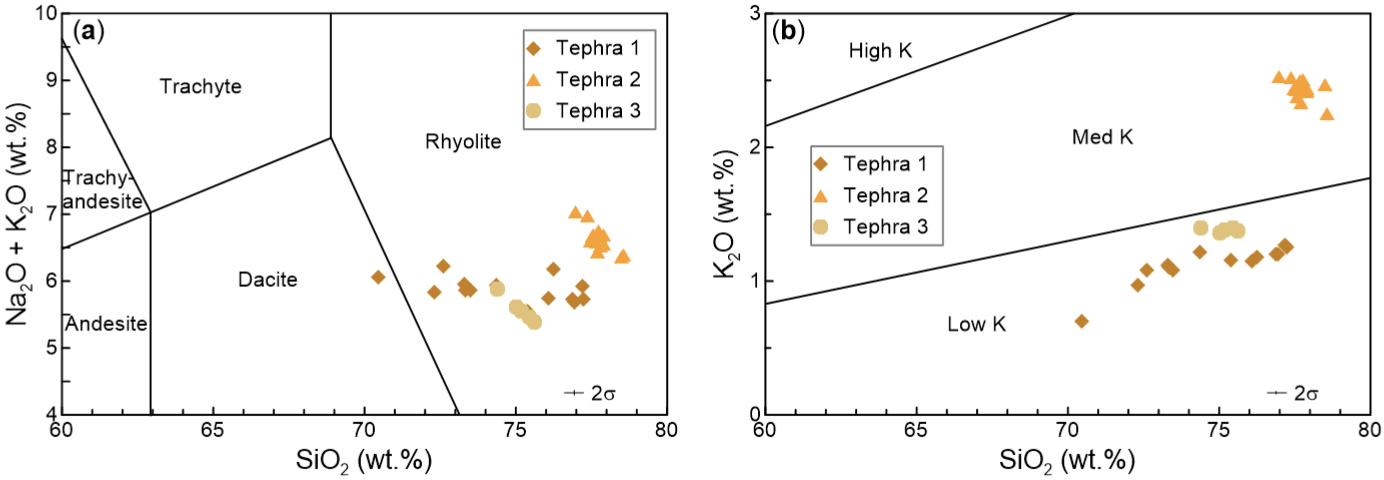
(a)
Tephra 1
Tephra 2
Tephra 3
Trachyte
Rhyolite
Trachy-
andesite
Dacite
Andesite
2σ
$Na_2O + K_2O$ (wt.%)
SiO_2 (wt.%)
(b)
High K
Med K
Low K
2σ
K_2O (wt.%)
SiO_2 (wt.%)

Figure 8

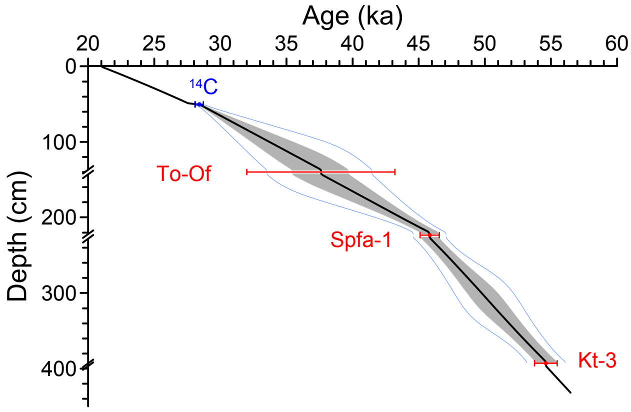
Age (ka)
20
25
30
35
40
45
50
55
60
0
100
200
300
400
Depth (cm)
^{14}C
To-Of
Spfa-1
Kt-3

Figure 9

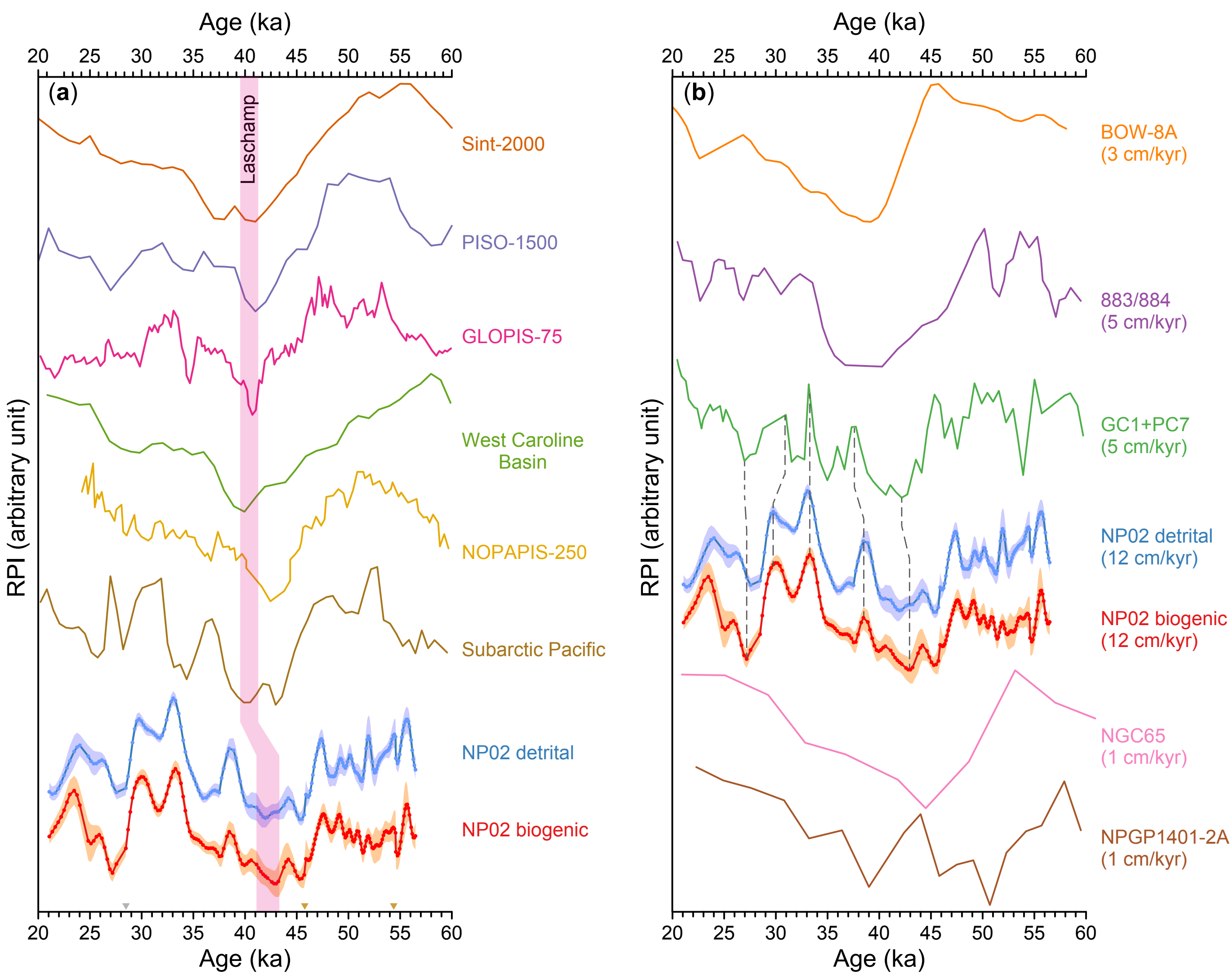

Age (ka)
20 25 30 35 40 45 50 55 60
(a)
Laschamp
Sint-2000
PISO-1500
GLOPIS-75
West Caroline Basin
NOPAPIS-250
Subarctic Pacific
NP02 detrital
NP02 biogenic
RPI (arbitrary unit)
Age (ka)
20 25 30 35 40 45 50 55 60
(b)
BOW-8A
(3 cm/kyr)
883/884
(5 cm/kyr)
GC1+PC7
(5 cm/kyr)
NP02 detrital
(12 cm/kyr)
NP02 biogenic
(12 cm/kyr)
NGC65
(1 cm/kyr)
NPGP1401-2A
(1 cm/kyr)